

UNIVERSITY OF CALIFORNIA

Los Angeles

Fabrication of Two-Dimensional Photonic Crystal Single-Defect Cavities and their
Characterization by Elastic Scattering

A dissertation submitted in partial satisfaction of the
requirements for the degree Doctor of Philosophy
in Electrical Engineering

by

Ivan Alvarado-Rodriguez

2003

The dissertation of Ivan Alvarado-Rodriguez is approved by

Ming Wu

Yahya Rahmat-Samii

W. Gilbert Clark

Eli Yablonovitch, Committee Chair

University of California, Los Angeles

2003

Table of Contents

1. Introduction and Motivation	1
2. Design of 2D Photonic Crystal Cavities	6
3. Fabrication of Two-Dimensional Photonic Crystal Cavities.....	14
4. Characterization of 2D Photonic Crystal Cavities by Photo-luminescence Spectrum Measurements.	32
5. Characterization of 2D Photonic Crystal Cavities by Elastic Scattering Measurements	50
6. Summary and Suggestions for Future Work: Prospects for Increasing Cavity Q	60
Appendix A: Extended Modes in 2D Photonic Crystal Films	66
Bibliography	71

Table of Figures

Figure 1.1: (a) Typical reflectivity spectrum of a photonic crystal. λ_1 and λ_c lie within the forbidden band-gap whereas λ_2 lies in the allowed propagation band. Several operations can be performed such as filtering (c), waveguiding (d) optical confinement (e) wavelength add/drop	3
Figure 1.2: Superprisms effect in 2D photonic crystals [3]	4
Figure 2.1: Two-dimensional photonic crystal slab where a is the lattice period, r is the hole radius, and t is the slab thickness.	7
Figure 2.2: Dispersion relation or band diagram for TE polarized light. The material has a refractive index of 3.4 and a filling ratio $r/a = 0.3$. The shadowed area is the forbidden photonic bandgap. Indicated are the guided modes, leaky modes, and light line of the slab [4].	8
Figure 2.3: Dispersion relation or band diagram for TM polarized light. The parameters are the same as in Fig. 2.2. No forbidden photonic bandgap is present for these modes [4].	9
Figure 2.4: Two-dimensional photonic crystal single defect cavity on a glass slide.	10
Figure 2.5: Computer simulation of the defect mode electromagnetic distribution: (a) top view (b) cross section [6].	11
Figure 2.6: Cavity resonance wavelength for several filling ratios r/a , of the photonic crystal. The resonance wavelength was calculated using FDTD and the structure shown in Fig. 2.4. The refractive indexes used were those corresponding to InGaAs and InP.	13

Figure 3.1: Summary of the process followed to fabricate 2D photonic crystals on semiconductor substrates. Each panel depicts the cross section of the processed sample after completion of the step.	15
Figure 3.2: (a) Electron beam impinging on resist produces secondary electrons. These electrons scatter in every direction around the exposed feature. (b) Areas of high and low dose in a 2D photonic crystal pattern. (c) Micrograph of the edge of a 2D photonic crystal written on PMMA. The granular surface is due to the gold sputtered on the resist.	18
Figure 3.3: Typical RIE reactor.	
Figure 3.4: Etching characteristics for PMMA and SiO ₂ .	21
Figure 3.5: SEM micrographs showing the undercut characteristic and the pattern transfer to SiO ₂ using the Oxford Plasmalab 80 RIE at low pressure and CHF ₃ as a reactant.	22
Figure 3.6: Typical configuration of an ion beam gun and CAIBE reactor.	23
Figure 3.7:(a) Ion milling of GaAs, InP, and SiO ₂ . (b) CAIBE of the same materials. The process parameters are the same in both cases except for the introduction of Cl ₂ into the chamber in the case of CAIBE.	24
Figure 3.8: Surface damage on an InP substrate by arc pitting.	26
Figure 3.9: Device layout on sample. The dimensions of each photonic crystal are 40×60 μm	28
Figure 3.10: Overall view of the fabricated 2D photonic crystal. The cavity location is at the center of the structure. The photonic crystal was fabricated with almost no unintentional defects.	28

Figure 3.11: Micrograph of one of the fabricated 2D photonic crystal cavities.	29
Figure 3.12: Close up of the holes etched into the semiconductor film.	29
Figure 3.13: Erosion in the SiO ₂ mask allow the sample to be attacked by skew ion rays. (b) Device fabricated using a 90nm thick SiO ₂ mask.	30
Figure 3.14: SiO ₂ mask made by the improved RIE process. Results of this process are shown in Figs. (3.11) and (3.12).	31
Figure 4.1: A photon is produced by electron-hole recombination inside the cavity region. The photon can be delivered into the photonic crystal leaky modes, the cavity mode, or the free-space radiation.	38
Figure 4.2: Experimental setup utilized in the photoluminescence characterization of the photonic crystal cavity.	40
Figure 4.3: Collected photoluminescence spectra when pump laser is focused on (a) cavity, (b) bulk photonic crystal (4 μm from cavity), (c) unpatterned region.	42
Figure 4.4: Photoluminescence spectra from cavities for different photonic crystal lattice parameters. The photoluminescence from the bulk photonic crystal is shown as reference. All the structures have the same void-filling factor of 35%. The signal fall off at the 1650 nm is due to the optical limit of the InGaAs photodetector used in the experiment.	43

Figure 4.5: Optical resonator filled with absorbing medium. The right side mirror is a perfect reflector whereas the left side mirror has a reflectivity very close to 1.	45
Figure 4.6: Measured absorption coefficient as a function of the photon energy in $\text{In}_{0.47}\text{Ga}_{0.53}\text{As}$. The intersection of the dashed line with the abscissa corresponds to the energy bandgap. The photoluminescence spectrum of the sample studied is shown in the inset [12].	47
Figure 4.7: Cavity quality factor $1/Q$ vs. absorption coefficient obtained from the data of Fig. (4.4). The lattice parameter of the photonic crystal is a and the cavity resonance wavelength is λ_0 .	48
Figure 5.1: Basic experimental setup for measuring elastic scattering.	51
Figure 5.2: Complete experimental setup for elastic scattering measurements. The sample is sandwiched by two long working distance microscope objectives. The light from an illuminator is sent through the system to image the devices on CCD camera. The two insets show the images seen on CCD camera and on long wavelength camera.	53
Figure 5.3: Scattering spatial map of the electromagnetic defect mode using light at $1.54 \mu\text{m}$. The 2D photonic crystal cavity is drawn at scale in the background as a reference. The device studied has a lattice period $a=500 \text{ nm}$ and a void filling factor of 35%.	55
Figure 5.4: Same as Fig. 5.3 but for a device with lattice period $a=525 \text{ nm}$ and a void filling factor of 35%. No resonance is measured in this case.	56

Figure 5.5: Scattering signal from cavity and background signal. The overall increase of the signal as a function of wavelength observed in both cases is due to the spectral response of the tunable laser. The device studied has a lattice period $a=500$ nm and a void filling factor of 35%.	58
Figure 5.6: Cavity's scattering spectrum relative to the background from the data shown in Fig. 5.5.	59
Figure 6.1: Photonic crystal defect cavity with modified dielectric constant.	62
Figure 6.2: Calculated energy stored in the cavity as a function of time. Reduction of the dielectric constant decreases the temporal decay of the energy stored [1].	63
Figure 6.3: Quantum-Well intermixing process. (a) A SiO ₂ film is patterned on top of an InGaAsP/InP multiple quantum well structure. The wafer is then thermally annealed. (b) The SiO ₂ film is removed. The dielectric constant of the structure is locally modified.	64
Figure 6.4: The SIMOX process. (a) Oxygen ions are implanted on a masked SOI wafer. (b) The mask is removed and the wafer is thermally annealed. SiO ₂ is formed in the exposed regions.	65
Figure A.1: Emission from a thin layer of photoluminescent material on a glass slide. The material can be the structure InP/InGaAs/InP studied in this thesis. (a) unpatterned thin film: part of the emission escapes while part is trapped; (b) thin film photonic crystal: the emission that is trapped can be extracted by Bragg diffraction.	67

- Figure A.2: Experimental setup for angle-resolved photoluminescence. The sample is pumped with a laser and the emission is collected on the opposite side. A spatial mask is used to select the angle. 68
- Figure A.3: Typical spectra obtained using angle-resolved photoluminescence. The spectra show the difference in polarization state of the emitted light. The reference is the photoluminescence obtained from the unpatterned semiconductor thin-film. 69
- Figure A.4: Map of the dispersion characteristic of the extended modes. The inset shows the Brillouin zone of the studied 2D photonic crystal. 70

Acknowledgements

I am very grateful to the people of the CONACyT-UC-MEXUS program; without their support, this work would not have been possible. I also thank Ivair Gontijo and Hans Robinson for many helpful discussions. Special acknowledgements and thanks to my advisor Prof. Eli Yablonovitch. This project has been supported by DARPA under the CHIPS program.

VITA

- 08/20/73 Born in Monterrey, Mexico
- 12/10/94 B.Sc. Physics ITESM Campus Monterrey Mexico
- 05/01/98 M.Sc. Optical Sciences INAOE SEP-CONACyT
Mexico
- 09/01/98 - 03/30/03 Graduate Student Researcher
University of California Los Angeles

Publications and Presentations

- I. Alvarado-Rodriguez, and E. Yablonovitch, *Separation of Radiation and Absorption Losses in Two-Dimensional Photonic Crystal Single Defect Cavities*, J. Appl. Phys. **92**, 11, (2002) 6399
- I. Alvarado-Rodriguez and Eli Yablonovitch, *2D Photonic Crystal Defect Cavities: Fabrication and Characterization*, Sixth International Conference on the Electrical Transport and Optical Properties of Inhomogeneous Media, Salt Lake City, UT July 2002
- I. Alvarado-Rodriguez, I. Gontijo, and Eli Yablonovitch, *Fabrication and Characterization of 2D Photonic Crystal Defect Cavities* (Invited paper), Proceedings of 2001 URSI International Symposium on Electromagnetic Theory, Victoria BC, Canada May 13-17 2001. Paper id MN-T23.23.
- I. Alvarado-Rodriguez, I. Gontijo, E. Yablonovitch. *Fabrication of Photonic Crystal Defect Cavities in 2D Photonic Crystals*, Photonic Crystals and Light Localization Workshop, Crete, Greece 2000.
- I. Alvarado-Rodriguez, P. Halevi, and Adán S. Sánchez, *Dipole radiation in a one-dimensional photonic crystal: TE polarization*, Phys. Rev. E., **63**, 5 (2001) 056613
- I. Alvarado-Rodriguez, P. Halevi and J.J. Sanchez-Mondragon, *Density of states for a dielectric superlattice: TE(s) polarization*, Phys. Rev. E, **59**, 2 (1999)
- I. Alvarado-Rodriguez, P. Halevi and J.J. Sanchez-Mondragon, *Radiation emission in inhomogeneous media: dipole between two plane-parallel mirrors*, Rev. Mex. Fis. **44**, (3) 268-276 (1998)

ABSTRACT OF THE DISSERTATION

Fabrication of Two-Dimensional Photonic Crystal Single-Defect Cavities and their
Characterization by Elastic Scattering

by

Ivan Alvarado-Rodriguez

Doctor of Philosophy in Electrical Engineering

University of California, Los Angeles 2003

Professor Eli Yablonovitch, Chair

The subject of this thesis is fabrication process development and characterization of two-dimensional photonic crystal single defect cavities. These devices are potential candidates to become one of the building blocks of photonic integrated circuits, which are expected to be valuable in optical telecommunications.

Photonic crystal cavities were designed based on results from the computer simulations, which were obtained from various sources. To make the cavities, a fabrication process, which involved sub-micron patterning and etching techniques, was developed. High quality structures were obtained after the optimization of the different parameters of the process.

Photoluminescence spectral measurements were used to observe the signature of the cavity mode in the structure. The theory of spontaneous emission in inhomogeneous media is presented to explain the experimental observations. This theory is applied to the photoluminescence exhibited by the semiconductor materials. From the photoluminescence spectral measurements, the cavity tuning and quality factor Q can be estimated. Absorption and Radiation loss mechanisms present in the cavities were separated by performing a curve fit of the loss rate, $1/Q$, versus the wavelength-dependent absorption coefficient of the material used. By extrapolating this curve to zero absorption, the radiation loss rate $1/Q_{\text{rad}}$ of the cavity is obtained.

An alternative characterization method based on elastic scattering of light was implemented. This method consists of the measurement of the spectrum of the light scattered from the cavity when a tunable light source is focused onto it. The wavelength dependence of the scattered light intensity can be used to estimate the cavity quality factor, Q , in a way similar to the photoluminescence spectrum measurements. This experimental method is useful to determine the maximum possible Q that occurs when the cavity does not absorb light at the cavity resonance wavelength.

1. Introduction and Motivation

1.1. Need for Photonic Integrated Circuits

One of the current challenges in the optical telecommunication industry is the production of photonic circuits in which several different operations can be performed effectively and at the lowest manufacturing cost. In this respect, the model of electronic integration applied to optics is the natural choice. The advantage of integration is the fact that many devices can be fabricated and arranged in different ways all simultaneously in one fabrication process, thereby reducing significantly the cost of packaging individual components. The latter is particularly costly in current fiber-based optical subsystems wherein most of the assembly is done by humans rather than by automation. Furthermore, the miniaturization provided by integration reduces the footprint of optical systems and subsystems.

Nevertheless, the trend towards miniaturization in electronics is different than that of optical systems. In CMOS electronics, for example, as the gate length is reduced, the overall speed and other performance characteristics of the circuit are increased. Geometrical dimensions play an important role in determining the light flow characteristics and power throughput in a particular optical circuit, and need to be controlled very accurately, as shall be seen in this dissertation thesis.

1.2. Two-Dimensional Photonic Crystals for Photonic Integrated Circuits

Photonic Crystals, the electromagnetic analog of semiconductor crystals, have stirred the imagination toward photonic integrated circuits. At the same time, the build-out of telecommunications infrastructure is creating a demand for large volumes of optical communications components and sub-systems. Integration at the tiniest scale of photonic crystals allows the largest number of components to be produced from a single wafer, reducing cost, and allowing considerable optical complexity.

Photonic Crystals are anisotropic optical media wherein the refractive index is a periodic function of the space [1,2]. According to the periodicity, photonic crystals can be one, two, or three-dimensional. Even though 3D photonic crystals have very interesting properties, it has been found that 2D photonic crystals are easier to fabricate since the procedure is similar to that used for planar electronic integrated circuits. Furthermore, 2D photonic crystals also provide functionality to steer and modify the flow of light in different ways.

One of the requirements for photonic integrated circuits is the need for system multi-functionality, i.e. the ability to perform different operations, under the same materials technology. This multi-functionality has been proposed for 2D photonic crystals arranged in different ways. Fig. (1.1) shows several proposed ways in which a 2D photonic crystal can be used. For instance, a pictorial sketch of the reflectivity spectrum from a 2D photonic crystal structure is depicted in Fig. (1.1)(a). This reflection property allows us to filter light at certain wavelengths while letting through others, as

shown in Fig. (1.1) (b). Using this reflection property, it is possible to guide light and steer it into different directions, as in Fig. (1.1) (c) [2]. This property also allows us to trap light at certain wavelengths forming an optical cavity, as depicted in Fig. (1.1) (d). The latter is the subject of this thesis. With this structure, it is also possible to put different pieces together and to form an optical add/drop demultiplexer, as in Fig. (1.1)(e).

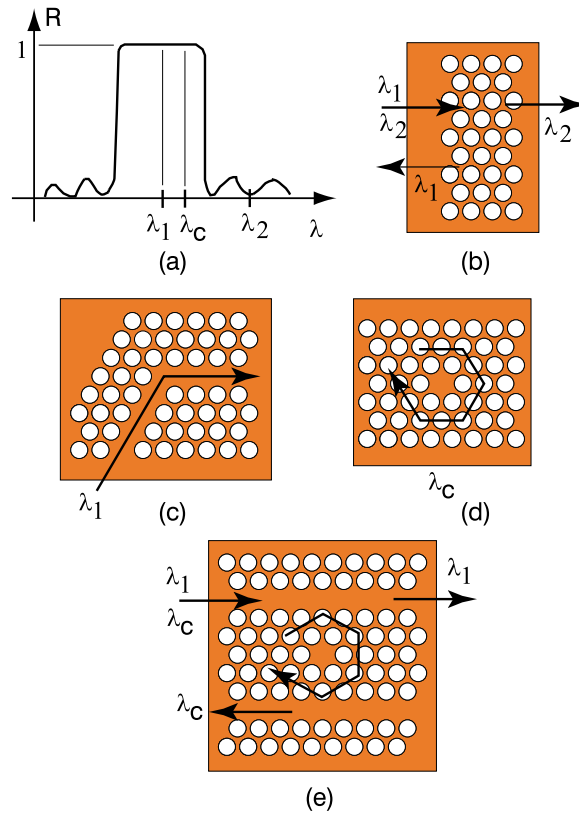


Figure 1.1: (a) Typical reflectivity spectrum of a photonic crystal. λ_1 and λ_c lie within the forbidden band-gap whereas λ_2 lies in the allowed propagation band. Several operations can be performed such as filtering (c), wave guiding (d) optical confinement (e) wavelength add/drop.

The prospect devices described above use the band-gap characteristic of the 2D photonic crystals. Other devices based on the dispersion properties have also been proposed. Fig. (1.2) shows how the dispersion properties of a photonic crystal can be used. Due to the high dispersion of wavelengths near the band edge, it is possible to separate the spectral contents of an incoming multi-wavelength signal. This particular device is known as a "superprism" [3].

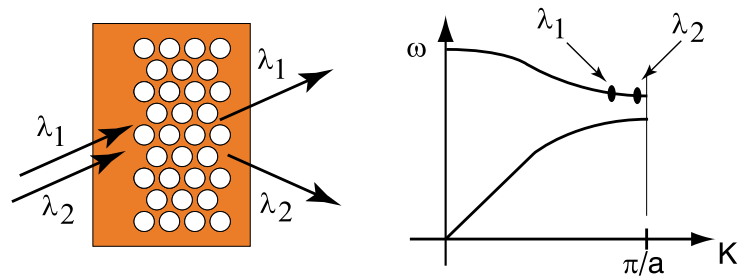


Figure 1.2: Superprisms effect in 2D photonic crystals [3]

In summary, several different operations have been proposed for 2D photonic crystals. It is important to note that all these devices are made in the same fabric, i.e. they are all based on a 2D periodic array of holes. This implies that the multi-functionality of 2D photonic crystals is allowed simply by adjusting the geometry of the structure itself and by joining several devices together to form complete integrated sub-system.

1.3. Work presented in this thesis

In this thesis, we have concentrated on the fabrication and characterization of 2D photonic crystal single defect cavities. These devices, in particular, are interesting due to

the potential of achieving a high cavity Q and, thus, they are promising for filtering applications in photonic integrated circuits.

In Chapter 2 of this thesis an overview of the cavity design is presented. The fabricated devices were based on designs obtained by numerical calculations. Chapter 3 describes the fabrication process and several issues concerning to the different steps of the process. Spontaneous emission modification and cavity characterization using photoluminescence is presented in Chapter 4. Characterization is aimed towards measuring the cavity Q, which is a function of the radiation and absorption losses of the cavity. A method to separate these losses is presented. Chapter 5 describes the characterization of the device by elastic scattering of light from the cavity. Conclusions and prospects to increase the cavity Q are presented in Chapter 6. In Appendix A, the extended modes of 2D photonic crystals are described based on previous experimental work carried out in our research group [4].

2. Design of 2D Photonic Crystal Cavities

2.1. Introduction

In this chapter, the design and theoretical considerations of a 2D photonic crystal cavity are presented. Since this thesis is mostly experimental, the numerical calculations are mentioned briefly, concentrating only on results pertinent to device design.

2.2. Basic Properties of Two-Dimensional Photonic Crystals

We focus our study on 2D photonic crystals formed by a periodic array of holes arranged in a triangular lattice fashion, as depicted in Fig. (2.1). As it was originally proposed [5], electromagnetic waves propagating in periodic dielectric structures behave in a similar way as electron waves in solid state crystals. This implies that the propagation of light is allowed at certain frequencies and forbidden to others. In the case of 2D photonic crystals, these properties apply to waves with wavevector components lying in the plane of the periodicity. The allowed propagation electromagnetic modes are the so-called Bloch waves, whose mathematical form is given by [5]

$$\mathbf{E}(\mathbf{r} + \mathbf{a}, t) = \mathbf{E}(\mathbf{r}, t)e^{i\mathbf{k}\cdot\mathbf{a}} \quad (2-1)$$

where \mathbf{a} is a primitive lattice vector, and \mathbf{k} is the wavevector component in the plane of the periodicity. Eq. (2-1) is a solution of the Maxwell equations for waves traveling in periodic dielectric structures.

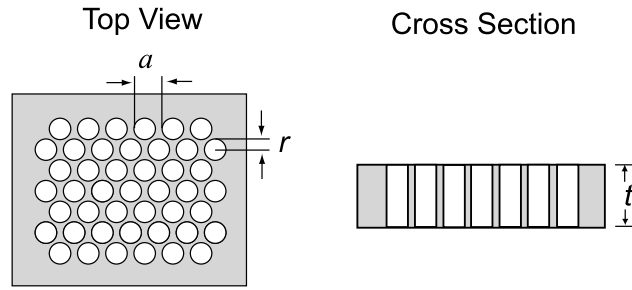


Figure 2.1: Two-dimensional photonic crystal slab where a is the lattice period, r is the hole radius, and t is the slab thickness.

A very important parameter in Eq.(2-1) is the wavevector \mathbf{k} and most of the research carried out in photonic crystals is aimed towards the calculation of \mathbf{k} as a function of the frequency, which is the dispersion relation. This relation is required in order to determine the location of the forbidden and allowed propagation bands.

There are no simple analytical methods to calculate the dispersion relation of a photonic crystal and the analysis has to be carried out aided by computational techniques used to solve Maxwell equations. Fig. (2.2) shows the dispersion diagram of a triangular 2D photonic crystal. In this figure, the propagation modes and the forbidden band are indicated for the TE modes, which have the electric field polarized parallel to the plane of the periodicity. The dispersion relation has been obtained using the plane wave expansion [6] in a periodic medium consisting of infinitely long air cylinders in a dielectric material. Fig. (2.3) shows the dispersion diagram for a TM polarized waves, which have the electric field polarized perpendicular to the direction of the periodicity. The main parameters of a 2D photonic crystal are the lattice constant (or lattice parameter) a and the filling ratio expressed as r/a . Modifying these parameters in any way will change the dispersion characteristics of the waves in the photonic crystal and, therefore, the location

of the propagation and forbidden bands. The slab thickness also influences the properties of the photonic crystal and, thus, additional adjustments of the geometry may be necessary to obtain a specific band gap location [7,8].

The propagation modes, which are also known as extended modes [2], subdivide into leaky modes and guided modes. Both modes propagate along the crystal exhibiting the dispersion characteristics shown in Figs. (2.2) and (2.3). The main difference is that the leaky modes in particular can couple to radiation modes outside the photonic crystal slab. These modes will be discussed with some detail in Appendix A. The guided modes, on the other hand, propagate along the periodic structure without escaping.

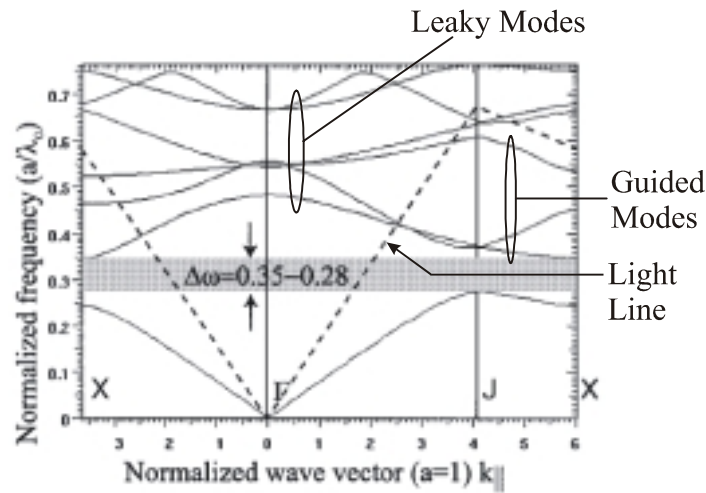


Figure 2.2: Dispersion relation or band diagram for TE polarized light. The material has a refractive index of 3.4 and a filling ratio $r/a = 0.3$. The shadowed area is the forbidden photonic bandgap. Indicated are the guided modes, leaky modes, and light line of the slab [8].

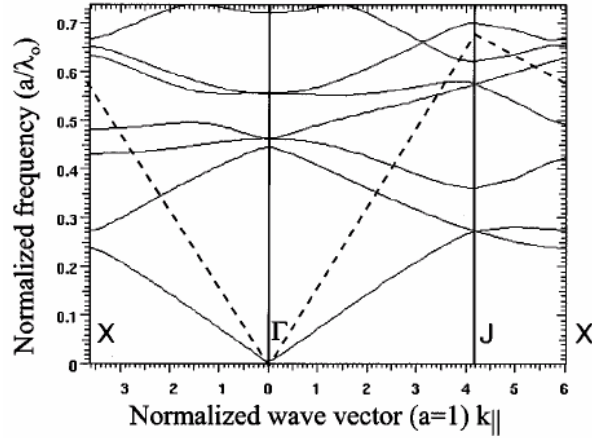


Figure 2.3: Dispersion relation or band diagram for TM polarized light.

The parameters are the same as in Fig. 2.2. No forbidden photonic bandgap is present for these modes [8].

Notice from the dispersion diagrams that, even though there is a full forbidden band for the TE polarization, there is no such for the TM polarization. It is possible to obtain a complete forbidden bandgap for this polarization by increasing the r/a ratio. It has been found by numerical calculation that the required ratio is 0.44. This ratio, however, is hard to obtain reliably in practice since it leaves very narrow reeks between the holes.

2.3. Two-Dimensional Photonic Crystal Cavities

A cavity can be formed in the 2D photonic crystal by plugging a single hole in the lattice. The disturbance created by the extra dielectric material will induce a spectrally localized state inside the forbidden band, very much like a defect level in a semiconductor crystal. This 2D photonic crystal cavity is depicted in Fig (2.4). Unlike the

work done on optical cavities based on photonic crystal free-standing membranes, we have carried out our work on cavities on a glass substrates. The latter reduces the overall optical confinement of the cavity but increases significantly the mechanical robustness of the device.

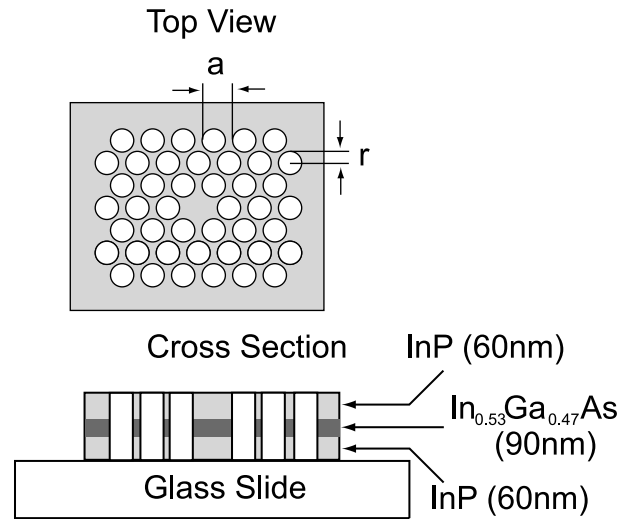


Figure 2.4: Two-dimensional photonic crystal single defect cavity on a glass slide.

In calculating extended modes in the allowed band, defect modes cannot be modeled by simple rules. Numerical methods must be used in order to obtain the spectral localization and the field distribution of the mode. Among the numerical techniques used to simulate defect modes, there is the super-cell method and the finite-difference time domain (FDTD) method, the latter being the most common technique. In FDTD, an initial field distribution is set in the structure and is numerically propagated in time until quasi-stable solutions are found. Figs. (2.5)(a) and (b) show the calculated field distribution of the defect mode.

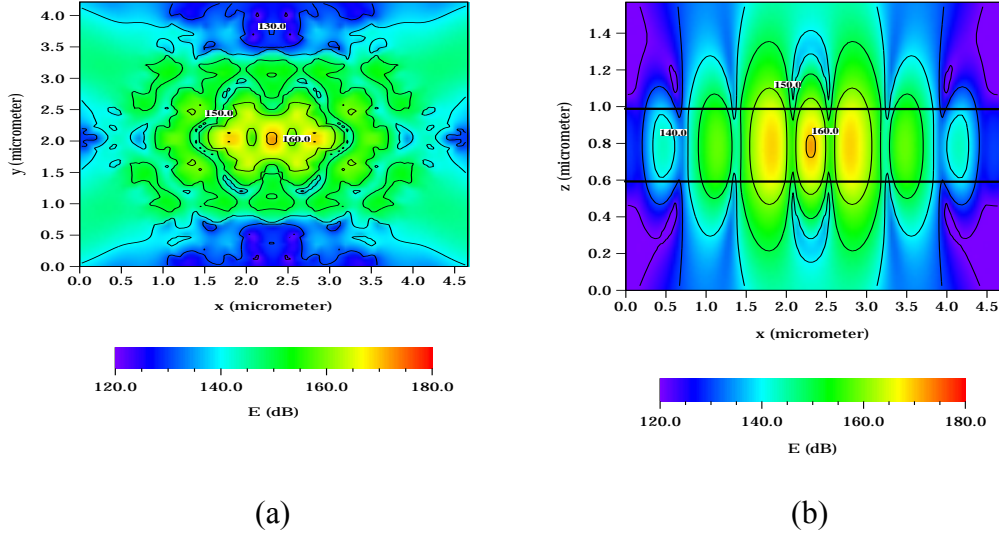


Figure 2.5: Computer simulation of the defect mode electromagnetic distribution: (a) top view (b) cross section [9].

As we mentioned, when a hole is plugged up in the photonic crystal, an optical cavity is formed in the horizontal direction. This, defect mode can be thought of as a cavity mode. As a simple explanation of this cavity formation, let us assume that an initial pulse of light sets off from this cavity and propagates in all in-plane directions. If the wavelength of the light lies within the bandgap, then the light is reflected back to where it originated. Choosing a proper lattice parameter will produce constructive interference of light, thereby forming a stable electromagnetic mode inside the forbidden gap.

The optical confinement of this cavity is provided by two mechanisms: vertical confinement and horizontal confinement. The vertical confinement is provided by waveguiding in the thin-film optical waveguide slab. Likewise, the horizontal confinement is due to reflections from the periodic structure. The former mechanism is due to the index

of refraction contrast in the air-semiconductor interface and the glass-semiconductor interface. It is clear that the energy confinement of this cavity is not perfect, as leakage exists vertically. To evaluate the degree of confinement of these structures, the quality factor Q has to be either calculated or measured. This shall be discussed in some detail in the following chapters of this thesis.

2.4. Cavity Tuning

The wavelength of the defect mode¹ or resonance wavelength can be tuned to different values by modifying the geometry of the photonic crystal. In Fig. (2.6) we plot the cavity wavelength versus the lattice parameter for different values of the filling ratio r/a . The wavelength range plotted is one portion of the wavelength range used in optical fiber communications. For instance, if the filling ratio $r/a = 0.31$ is chosen, then the lattice parameter can be adjusted may be moved from about 470 nm to 510nm in order to tune to a wavelength within the optical telecommunications band.

¹ Strictly speaking, optical frequency should be used instead of wavelength. However, most of the technical data in optics is given as a function of the free-space wavelength that corresponds to a certain optical frequency.

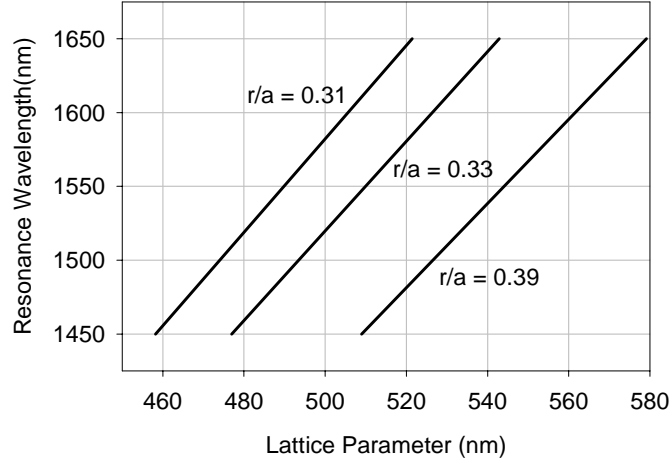


Figure 2.6: Cavity resonance wavelength for several filling ratios r/a , of the photonic crystal. The resonance wavelength was calculated using FDTD and the structure shown in Fig. 2.4. The refractive indexes used were those corresponding to InGaAs and InP.

3. Fabrication of Two-Dimensional Photonic Crystal Cavities

3.1. Introduction

This chapter is intended to explain the 2D photonic crystal cavity fabrication procedure. Even though there are several fabrication recipes proposed by different research groups, they vary significantly from facility to facility. The reason for that is the fact that equipment is not the same and it is operated under different conditions. It is always the case that extra effort is involved in developing a process that is new for the facility in which it is to be carried out.

3.2. Summary of the fabrication process

The fabrication procedure can be summarized as shown in Fig (3.1). Each step of the process will be described in detail in the following sections of this chapter. First we start with an InP/In_{0.53}Ga_{0.47}As/InP double heterostructure grown on an InP substrate. The layers were grown by metal-organic chemical vapor deposition (MOCVD). We then deposit SiO₂ by plasma enhanced chemical vapor deposition and we coat the surface with a layer of polymethylmethacrylate (PMMA). The cross-section of the wafer after the deposition and coating is shown in Fig. (3.1) (a). The PMMA layer is then patterned using electron beam lithography. After developing, the sample looks like Fig. (3.1) (b). Then, the sample is subjected to two different dry etching processes.

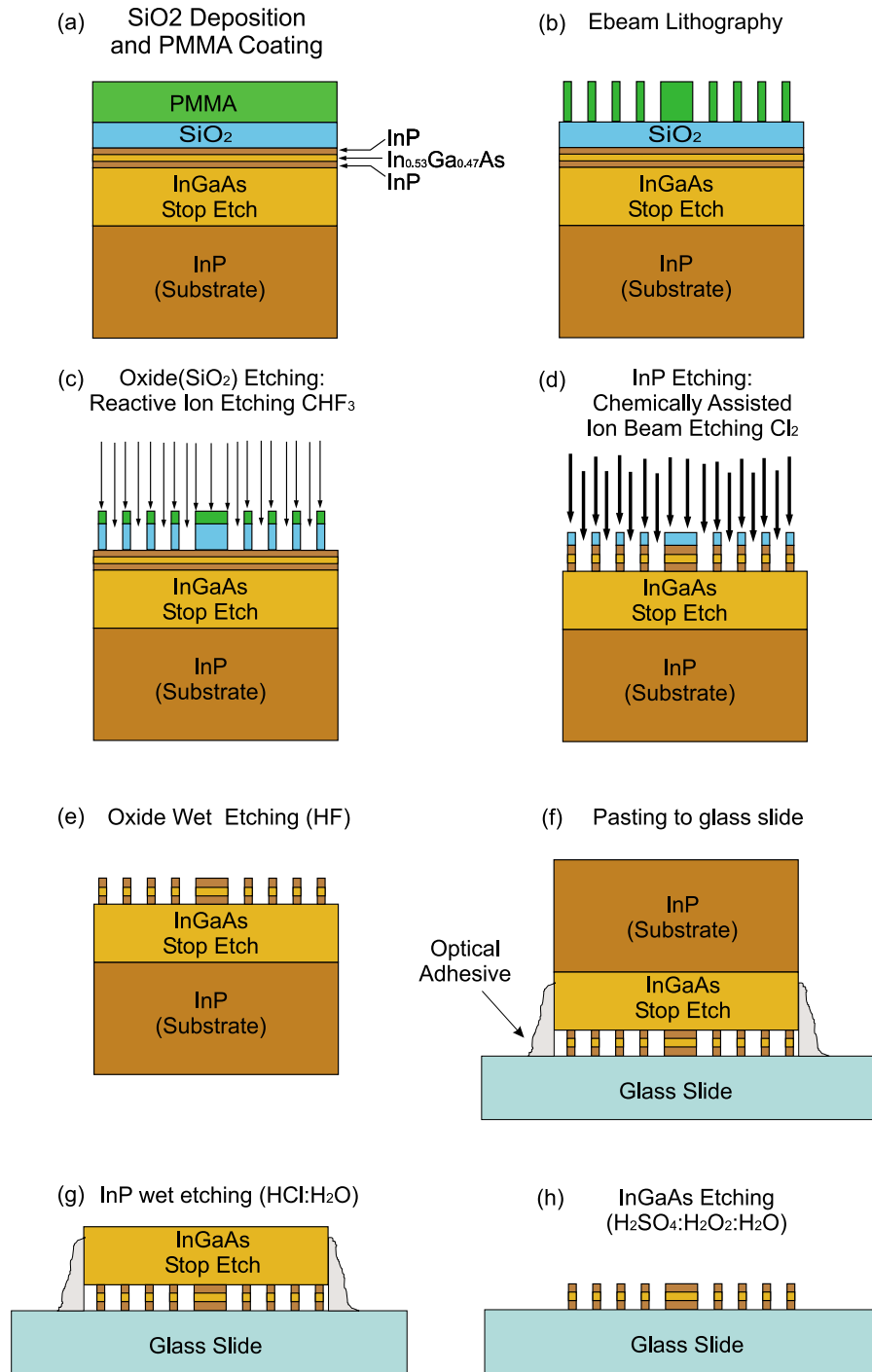


Figure 3.1: Summary of the process followed to fabricate 2D photonic crystals on semiconductor substrates. Each panel depicts the cross section of the processed sample after completion of the step.

The first etch transfers the pattern from the PMMA to the SiO₂ layer and the second etch transfers it to the semiconductor layers (Figs. (3.1) (c) and (d)). The remnants of the SiO₂ after the etching processes are removed away by wet etching using hydrofluoric acid (HF) (Fig. (3.1) (e)). The sample is pasted upside down on a glass slide and the InP substrate removed by two subsequent wet etching processes, as shown in Figs. (3.1) (f), (g), and (h).

3.3. Sample Preparation

The surface of the sample is cleaned using several solvents, namely, TCE, acetone, and methanol. Then a layer of about 200nm of SiO₂ is deposited by PECVD following a standard oxide recipe in a Plasmatherm 790 system. After the deposition, the surface is coated with polymethylmethacrylate (PMMA), which is a polymer sensitive to UV radiation and electron beam. The PMMA used is MicroChem 495,000 molecular weight diluted in Chlorobenzene at 4%. The polymer is spun on the sample for 40 secs at 4000 rpm. The resist is then baked in an oven at 180C for 30 minutes in order to dry off the solvent. The PMMA coating step is repeated to achieve a total layer thickness of 400nm.

3.4. Electron Beam Lithography

As seen in the previous chapter, photonic crystals operating in the optical regime are structures with geometrical parameters (such as lattice period and element size) of the

order of half the wavelength. Since the target vacuum wavelength is $1.55\mu\text{m}$, the fabrication process should involve lithography capable of patterning sub-micron features. The lithography method of choice in this case is electron beam lithography. This technique consists of an electron beam impinging on an electron-sensitive material. In this case, the material (or resist) is PMMA. The electron beam is scanned across the sample according to a computer generated pattern. Upon contact with high-energy electrons, the polymer bonds are broken, thereby increasing the solubility of the polymer resist to the developer. It is important to mention that the critical feature sizes of these structures can easily be obtained by current photolithography techniques, which are widely used in industry. Due to the great cost of the equipment required, such processes are used for mass production rather than device prototyping.

The patterns were written by a Leica EBL 100 set to a 50kV accelerating voltage and 30pA beam current. The optimum dosage range was $400\text{-}500\ \mu\text{C}/\text{cm}^2$. The samples were developed by immersing them into a solution of Deionized Water and Methylisobutylketone (concentration 3:1) for 30 secs.

One of the issues of electron beam lithography is the so-called *proximity effect*. This effect is depicted in Fig. (3.2). As the electron beam exposes the resist, secondary electrons are produced in the resist and in the substrate. These electrons are scattered in every direction, thereby exposing the vicinity of the desired feature. For close enough features, the dose due to secondary electrons builds up producing undesired exposure. In the case of 2D photonic crystals, this effect is particularly notorious at the edges of the

device, where the dose build up is much less than in the bulk, as shown in Figs. (3.2)(b) and (c). Even though the same dose is applied to the entire structure, the holes in the bulk receive a higher dose due to the build up generated by the surrounding holes. On the other hand, the holes at the edges of the structure receive a lower electron dose. To compensate for this effect, the electron beam dosage should be gradually increased towards the periphery of the device.

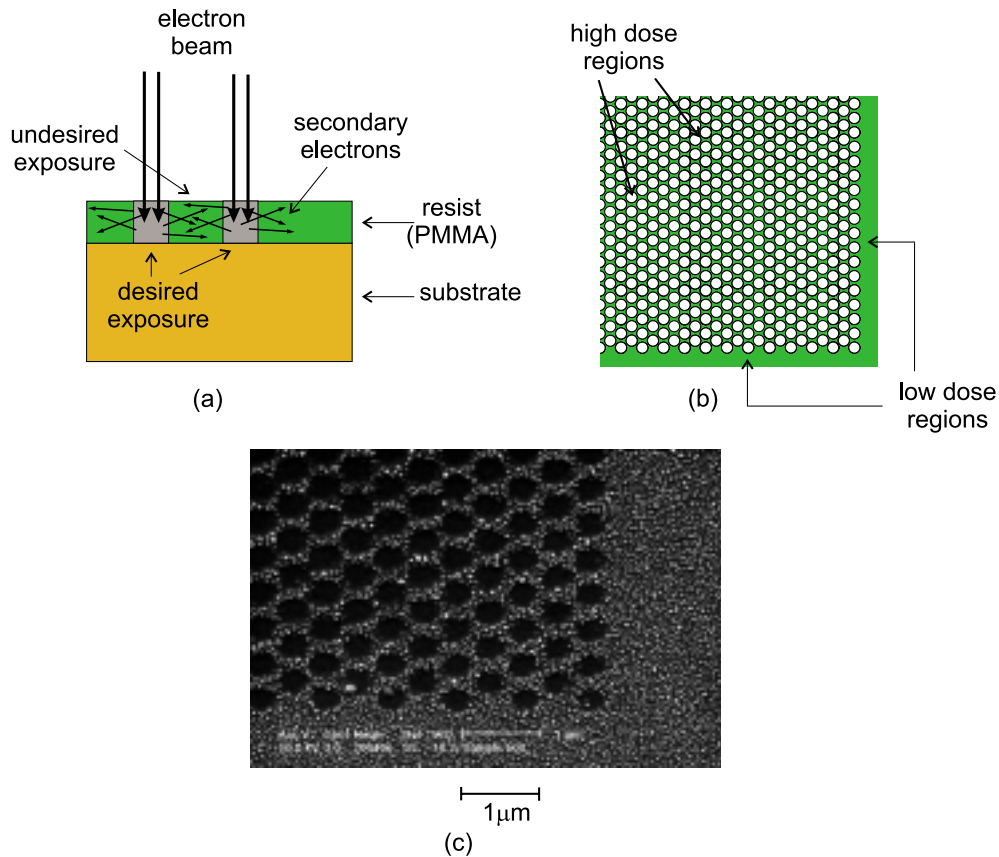


Figure 3.2: (a) Electron beam impinging on resist produces secondary electrons. These electrons scatter in every direction around the exposed feature. (b) Areas of high and low dose in a 2D photonic crystal pattern. (c) Micrograph of the edge of a 2D photonic crystal written on PMMA. The granular surface is due to the gold sputtered on the resist.

3.5. Oxide Etching: Reactive Ion Etching

Reactive ion etching (RIE) refers to any process in which an RF induced plasma generates reactive species that then serve to chemically etch material in immediate proximity to the plasma [10]. The typical configuration of RIE reactor is shown in Fig.(3.4). The reactor consists of a chamber with electrodes at the top and bottom. The reactive species are typically injected from the top electrode and the plasma is generated by applying a high power RF signal to the electrodes. The reactive gases commonly used in RIE are CF_4 , SF_6 , O_2 , Ar, and CHF_3 .

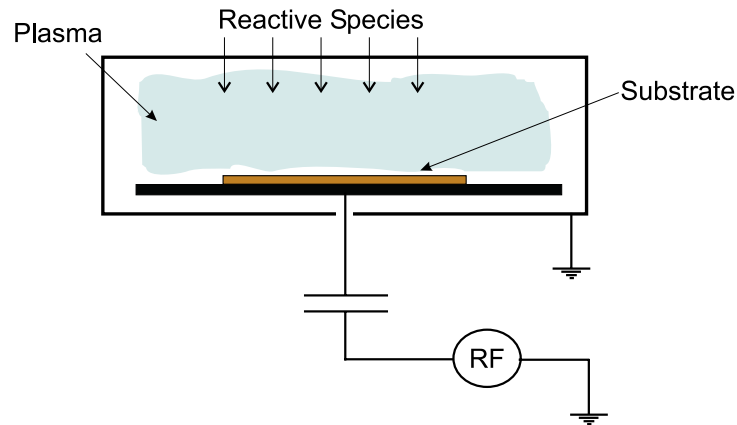


Figure 3.3: Typical RIE reactor.

One of the problems encountered in microfabrication is the effective transfer of very small features into semiconductor films and substrates. In RIE, this is especially problematic when the masking resist is particularly weak toward withstanding dry etching and the feature size is smaller than the thickness of the film into which we desire to transfer a the pattern. Particularly for 2D photonic crystals, different techniques have been developed. Those have involved the use of sequential masking materials into which

the pattern is transferred [11-13]. This problem is rooted in the fact that PMMA, which is the resist used in electron beam lithography, is not a hard material and, is eroded in the strong etching process required for GaAs or InP. These latter processes will be described shortly in this chapter.

For effective pattern transfer in RIE, using PMMA as a masking material, it was suggested in [14] to use CHF₃ as a reactive gas in a low background (or base) pressure (~10 μTorr). Etch pressure should also be low (~10mTorr) in order to achieve the transfer of nanoscale size features. These machine operation conditions are aimed to reduce the PMMA etch rate. The chemical reaction involved in the CHF₃ plasma during RIE produces less free fluorine concentration due to the formation of the radical HF in the gas phase, which is not easily dissociated. This reduction in the free fluorine concentration will decrease the formation of volatile compounds such as CF₄ on the PMMA surface, thereby reducing the overall PMMA etch rate. Another advantage of the CHF₃ plasma is that it reacts with the PMMA to produce a fluoropolymer, which stays on the surface of the mask. Low background pressure is also important because it reduces the Oxygen concentration in the chamber. It is known that Oxygen during a plasma process reacts easily with PMMA to produce CO volatile radicals and, thus, destroying the PMMA mask. Acceptable Oxygen concentrations are obtained if the etching process is carried out at background pressures of the order of 10 μTorr. The use of this particular etching process significantly improved the quality of the fabricated photonic crystals.

In our case, we desire to transfer the pattern that was created by electron beam lithography to a 200nm film of SiO₂, as shown in Fig. (3.1)(c). In the next section, it will

be determined that this oxide thickness will ensure a good pattern transfer onto the semiconductor thin film. As discussed in the previous chapter, for a device operating at optical wavelengths in the $1.55\mu\text{m}$ region, a typical lattice parameter and hole diameter are 500nm and 310nm , respectively; thus, the critical feature size is 190nm . Even though dry etching inherently provides high etch directionality (etch anisotropy) and good etch rate, particular care should be exercised in order to transfer a pattern from PMMA to SiO_2 . For an effective pattern transfer, two issues must be considered: etching undercut and etching transfer ratio. The former is controlled by the plasma pressure and power in an RIE system, and the second one by the chemistry of the reactants used in the process.

The machined used to perform the RIE was an Oxford Plasmalab80 set to the following operation parameters: reactive chemical CHF_3 , plasma power= 100W , and etch pressure= 0.015 torr. The etching transfer ratio is shown in Fig. (3.4).

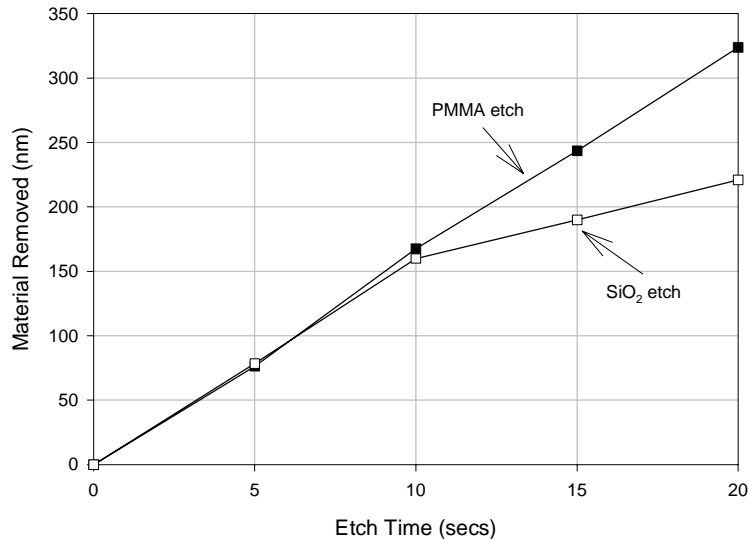


Figure 3.4: Etching characteristics for PMMA and SiO_2 .

As can be evidenced from the plot, the etch rate for pmma and SiO₂ are similar for times shorter than 10 secs which implies a 1:1 etch transfer rate. For longer etching times, the SiO₂ etch rate decreases. Also from the plot it can be determined that 17 secs are required to etch about 200nm which implies that the masking PMMA should be, at least, 270nm thick. In practice, the mask should be even thicker as other etching effects, such as non-uniformity and erosion, take place. As mentioned above, our samples were coated with 400nm thick PMMA.

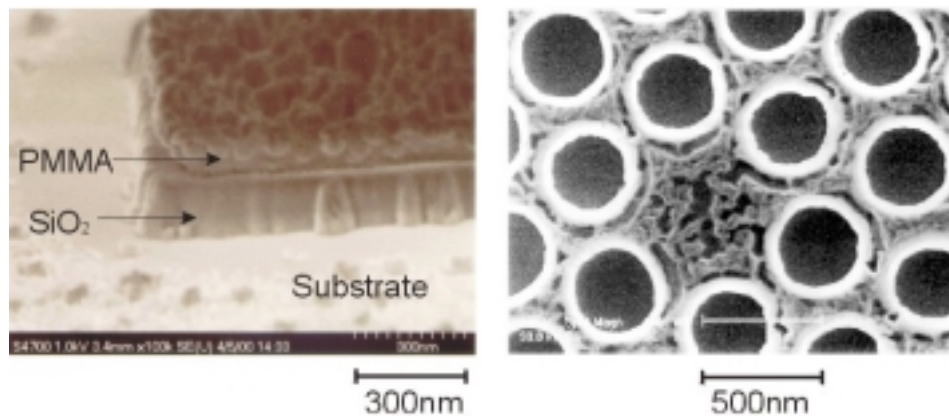


Figure 3.5: SEM micrographs showing the undercut characteristic and the pattern transfer to SiO₂ using the Oxford Plasmalab 80 RIE at low pressure and CHF₃ as a reactant.

Fig. (3.5) (a) and (b) show the etch undercut and the feature size achieved by setting the RIE to parameters specified above. As can be seen from the figures, features of the order of 100nm are achieved while maintaining an almost negligible undercut.

3.6. Semiconductor Etching: Chemically Assisted Ion Beam Etching

As mentioned in the previous section, RIE is a technique that relies mostly on a chemical reaction to remove material. This chemical reaction is often kinetically assisted by the introduction of ions. Chemically Assisted Ion Beam Etching (CAIBE) is a dry etching technique that relies mostly on physical etch, which is the removal of material from a substrate by collisions of ions impinging on its surface.

CAIBE, as its name implies, is assisted by a chemical reaction. Fig. (3.6) depicts the operation of the CAIBE process. Free electrons are produced in the cathode's filament and accelerated towards the anode. Ar is ionized by collisions with the free electrons and accelerated towards the accelerator grid. The beam is then neutralized by the addition of free electrons at the output of the accelerator grid. Electron neutralization is required to prevent the ion beam from expanding. Even though electrons are *reinject*ed into the ion beam, the *recombination* distance of ions with electrons is much larger than the distance between the ion gun and the target to be etched.

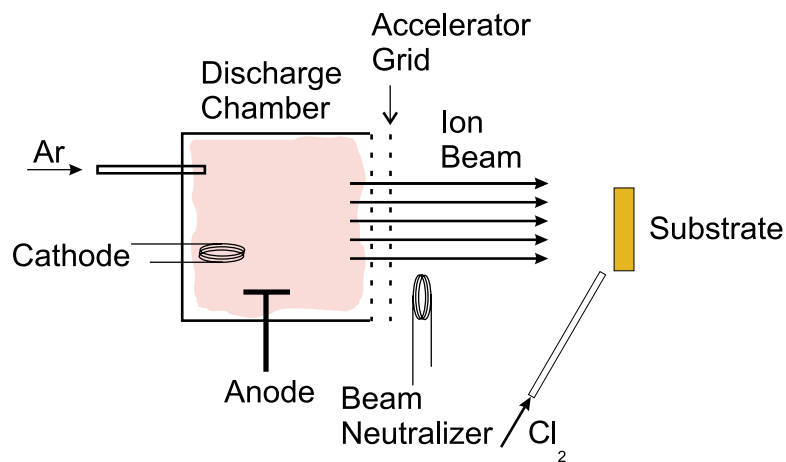
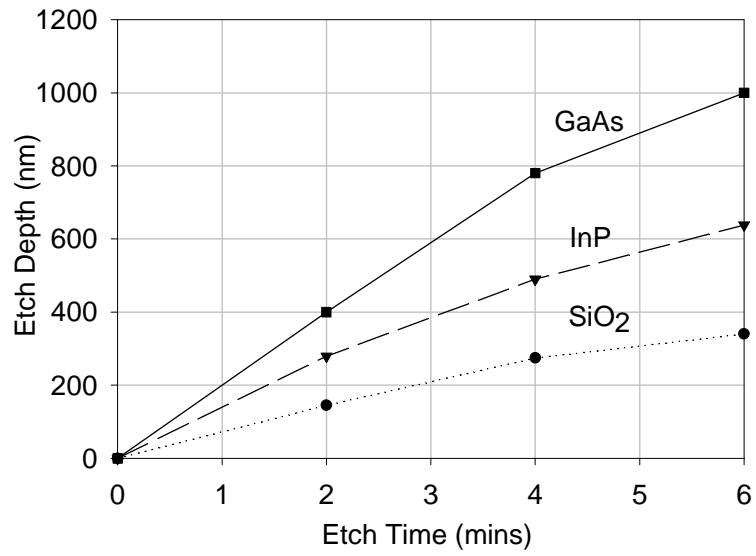
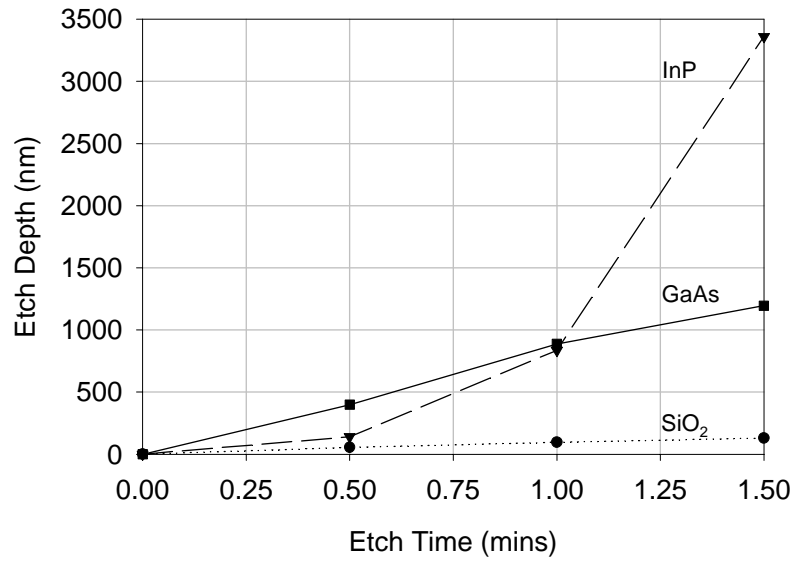


Figure 3.6: Typical configuration of an ion beam gun and CAIBE reactor.



(a)



(b)

Figure 3.7:(a) Ion milling of GaAs, InP, and SiO₂. (b) CAIBE of the same materials. The process parameters are the same in both cases except for the introduction of Cl₂ into the chamber in the case of CAIBE.

One of the main distinctions between kinetically assisted RIE and CAIBE is the fact that in RIE the chemical reaction produces highly volatile radicals whereas in CAIBE stable molecules are required to remove material. From that point of view, chemical etching in RIE is the dominant etching mechanism whereas physically assisted etching is dominant in CAIBE.

CAIBE is a modification of a dry etching process called Ion Milling. Ion Milling is a physical removal of material by collisions of energetic ions. The CAIBE system used in our fabrication is a home-made system consisting of a high-vacuum chamber and an ion gun. The system conditions were as follows: base pressure= $8\text{E-}7$ torr, Ar Flow = 3 sccm, Beam Current = 30 mA, Beam Energy = 1500 eV, Cl Flow = 2 sccm. The typical etching time was of 45 seconds.

Figs. (37) (a) and (b) show the etching characteristics for the Ion Beam Machine operating as Ion Milling or as CAIBE. Do notice the difference in time and etch depth scales. These figures show the advantage of etching assisted by Cl_2 . The interesting part here is that, even though the etch rates for GaAs and InP are dramatically increased, the etch rate for SiO_2 remains basically the same. This means that Cl_2 is not reacting chemically with SiO_2 so that the etching mechanism remains purely mechanical. Thus, adding Cl into the etching process increases the etch rate of GaAs and InP over SiO_2 . Another feature in Figs. (3.7) (b) is the nonlinearity in the etching rate exhibited by InP. This is due to heat produced in the sample by the action of the physical etching. One of

the ways to increase the etching rate in substrates like InP is by directly heating the substrate to be etched.

One of the most serious issues in CAIBE is the so-called *arc-pitting* effect. This effect is the result of either a poorly neutralized ion beam or an improperly grounded substrate holder in the chamber. As the ion etching proceeds, the substrate charges up significantly up to a point at which the insulation provided in the chamber is broken and the substrate discharges into the walls of the chamber or the holder itself. As a result of that, a micro-scale lightning occurs and a pit is burned into the substrate. Fig. (arc-pitting) shows the surface of a substrate damaged by arc-pitting.

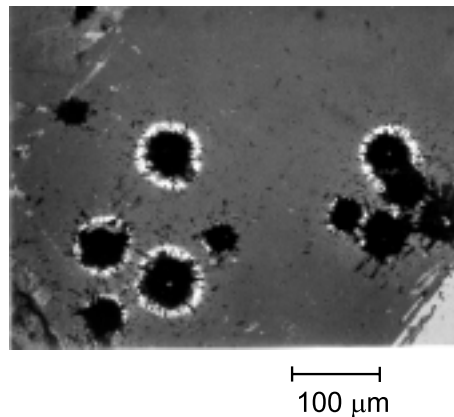


Figure 3.8: Surface damage on an InP substrate by arc pitting.

3.7. Device transfer to a Glass Slide

As shown in Fig. (3.1), after the dry etching process, the etched structure is transferred onto a glass slide. The sample is pasted upside down on a glass slide using Norland 70 optical adhesive and cured under UV light for 20 mins. The InP substrate is

etched away by dipping the sample in a solution of HCl:H₂O 3:1. The typical etching time is about 1 hr. to remove a substrate 600 μm thick. The etching stops at the InGaAs layer. This layer is subsequently etched away with a solution of H₂SO₄:H₂O₂:H₂O 1:8:500. The etching time in this case was 20 mins. to etch a 1 μm thick layer of InGaAs.

3.8. Fabricated sample

Fig. (3.9) shows the typical layout of the fabricated sample. Several devices were written on the film with a slight increment in the electron beam dose. The overall size of the photonic crystal area was of 40×60 μm. The fabrication technique allowed us to obtain a large photonic crystal surrounding the cavity with almost negligible defects across an area relatively large compared to the optical cavity (save for the intentional defect that makes the optical cavity). A micrograph of the surface of a 2D photonic crystal is shown in Fig. (3.10).

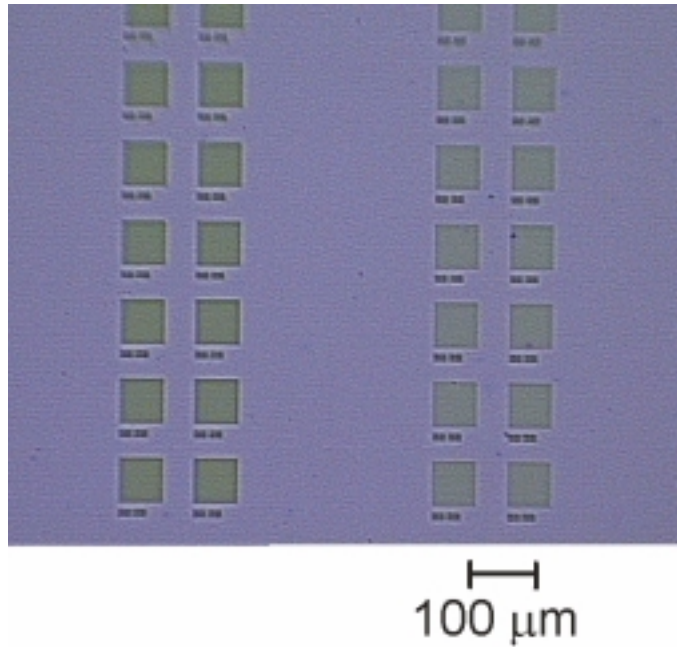


Figure 3.9: Device layout on sample. The dimensions of each photonic crystal are $40 \times 60 \mu\text{m}$.

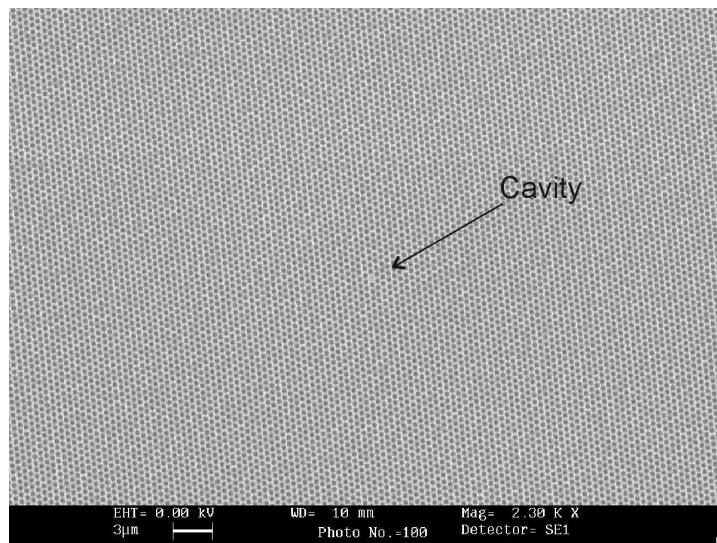


Figure 3.10: Overall view of the fabricated 2D photonic crystal. The cavity location is at the center of the structure. The photonic crystal was fabricated with almost no unintentional defects.

A closer look of the 2D photonic crystal cavity is shown in Figs. (3.11) and (3.12). As evidenced in these figures, good quality 2D photonic crystals were achieved.

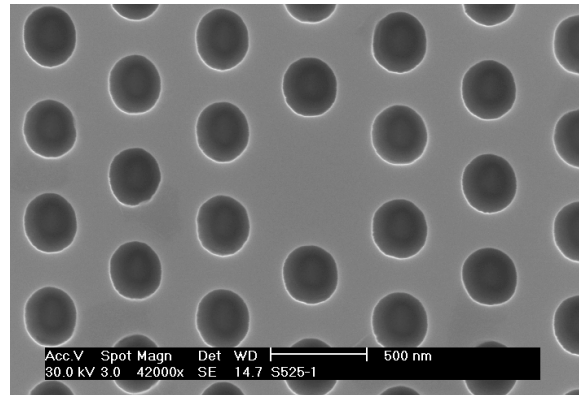


Figure 3.11: Micrograph of one of the fabricated 2D photonic crystal cavities.

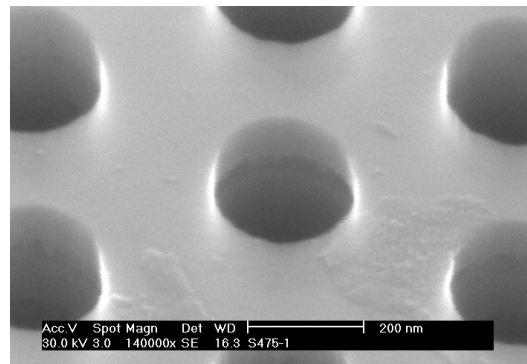


Figure 3.12: Close up of the holes etched into the semiconductor film.

3.9 Fabrication Improvement via RIE

As mentioned before, the quality of the fabricated structures was improved by the oxide mask etching described in section 3.6. One of the problems of CAIBE is the *mask erosion*, that is depicted in Fig. (3.13)(a). As the CAIBE etching proceeds, the edges of the oxide mask tend to etch faster and, thus, the veins in the mask assume a triangular

cross-section. This creates a window for skew rays in the ion beam that would be screened out otherwise. These rays severely affect the quality of the fabricated device as they attack the walls of the structure and create roughness on the surfaces. For example, in Fig. (3.13) (a), a SiO₂ mask was made following a process similar to the one described in section 3.6, but using CF₄ as the reactive chemical and a process pressure of 100 mtorr. Under these conditions, a maximum oxide thickness of 90nm is achieved if a PMMA mask of 400nm thick is used as a masking material. After CAIBE, the etched structure looks as in Fig. (3.13) (b).

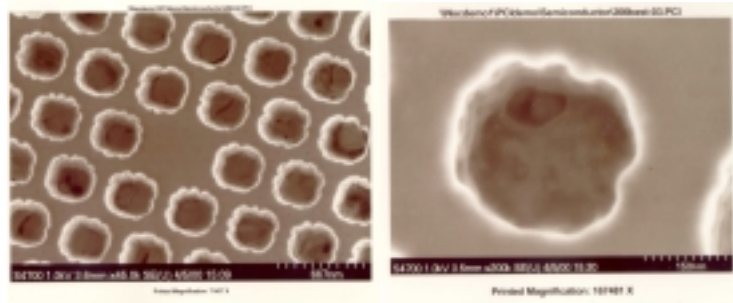
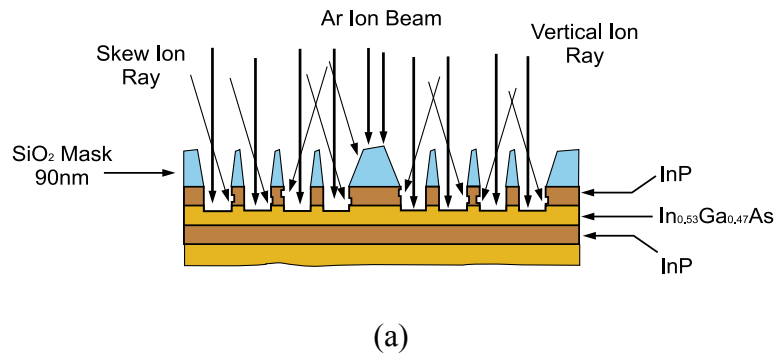


Figure 3.13: Erosion in the SiO₂ mask allow the sample to be attacked by skew ion rays. (b) Device fabricated using a 90nm thick SiO₂ mask.

The natural way to solve this problem is to make a thicker mask. This, however, is only possible if an RIE system with the right chemistry and operating pressure is

available. The RIE process described in section 3.6 allowed us to obtain a thicker mask and, thus, the mask erosion does not affect the quality of the device, as shown in Fig. (3.14). The fabrication results of this particular mask are shown in Figs. (3.11) and (3.12).

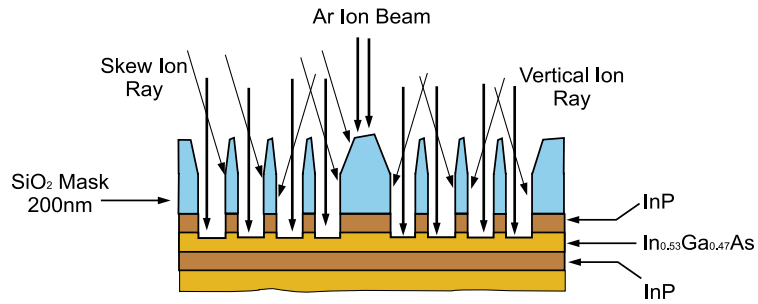


Figure 3.14: SiO₂ mask made by the improved RIE process. Results of this process are shown in Figs. (3.11) and (3.12).

4. Characterization of 2D Photonic Crystal Cavities by Photo-luminescence Spectrum Measurements.

4.1. Introduction

The characterization of 2D photonic crystals has been made mostly by measuring the spectrum of photoluminescence [15-17] and electroluminescence [18]. These techniques are useful and relatively easy to perform due to the fact that the light is generated inside the cavity and, thus, light coupling into the photonic crystal modes is very strong. In this chapter, the theory of modification of spontaneous emission is described and applied to the experimental results of light emission from 2D photonic crystal cavities. The theory of the cavity quality factor Q is also presented to estimate the radiation and absorption losses in the fabricated photonic crystal cavities.

4.2. Spontaneous Emission Theory of a Two-Level Atom

Spontaneous emission refers to the decay of an excited atom to a lower energy state, in the absence of incident electromagnetic radiation, with the subsequent production of a photon. Even though several classical and semi-classical models can be used to describe spontaneous emission, rigorous modeling requires second quantization theory, which means that both the atom and the field must be quantized.

We start by considering a quantum mechanical system consisting of a two-level atom and a multi-mode electromagnetic field. In our case, we can describe the system

using the following quantum mechanical states: $|2, \{0\}\rangle$ representing the atom in its excited state immersed in a vacuum electromagnetic field, and $|1, \{1_k\}\rangle$ representing the atom in its ground state and a photon delivered into any of the allowed photon modes (labeled as k) of the environment.

The interaction Hamiltonian of this system is given by [19]

$$H_I = -i \sum_k \left(\frac{\hbar \omega_k}{2} \right)^{1/2} \left(a_k \sigma_{21} \boldsymbol{\mu} \cdot \mathbf{A}_k - a_k^* \sigma_{21} \boldsymbol{\mu}^* \cdot \mathbf{A}_k^* \right) \quad (4-1)$$

where ω_k is the frequency of the k th electromagnetic mode, a_k (a_k^*) are the destruction (creation) field operators, σ_{21} is the dipolar moment operator, and $\boldsymbol{\mu} \cdot \mathbf{A}_k$ represents the dipole-field interaction energy. The interaction energy depends on the dipole moment exhibited by the radiation system, which could be an electronic transition in an atom, a band-to-band electronic transition in a direct bandgap semiconductor, etc. For convenience, we have expressed the field as a set of normalized eigenmodes of the vector potential. If the energy separation of the two levels of the atom is $\hbar \omega_o$, then the quantum state vector of the system can be expressed as

$$|\Psi\rangle = C_2(t) e^{-i\omega_o t} |2, \{0\}\rangle + \sum_k C_{1,k}(t) e^{-i\omega_k t} |1, \{1_k\}\rangle \quad (4-2)$$

where $|C_2(t)|^2$ is the probability of the atom to be in the excited state and $|C_{1,k}(t)|^2$ is the probability of the atom to be in ground state and a photon delivered into the k th mode.

Thus, due to the normalization condition for the state vector in eq. (4-2), we have that

$$|C_2(t)|^2 + \sum_k |C_{1,k}(t)|^2 = 1. \quad (4-3)$$

The time evolution of coefficients $C_1(t)$ and $C_2(t)$ can be obtained using the general equation of motion for quantum states [19]

$$i\hbar \frac{d}{dt} C_n(t) = \sum_m \langle n | H_I | m \rangle e^{i\omega_{nm}t} C_m(t) \quad (4-4)$$

where n and m represent either the state $|2, \{0\}\rangle$ or the state $|1, \{1_k\}\rangle$, and $\omega_{nm} = \omega_n - \omega_m$ is the corresponding energy difference between the states. Substituting eqs. (4-1) and (4-2) into eq. (4-4), we get

$$\frac{d}{dt} C_2(t) = \frac{1}{\hbar} \sum_k \left(\frac{\hbar\omega_k}{2} \right)^{1/2} \boldsymbol{\mu} \cdot \mathbf{A}_k C_{1,k}(t) e^{i(\omega_o - \omega_k)t} \quad (4-5)$$

$$\frac{d}{dt} C_{1,k}(t) = -\frac{1}{\hbar} \left(\frac{\hbar\omega_k}{2} \right)^{1/2} \boldsymbol{\mu}^* \cdot \mathbf{A}_k^* C_2(t) e^{-i(\omega_o - \omega_k)t}. \quad (4-6)$$

Eqs. (4-5) and (4-6) are the time-evolution equations for the quantum state vector given in eq. (42). Integrating eq. (4-6) and substituting into eq. (4-5), we have that the time-evolution of the upper state is given by

$$\frac{d}{dt} C_2(t) = -\frac{1}{2\hbar} \sum_k \omega_k |\boldsymbol{\mu} \cdot \mathbf{A}_k|^2 \int_{t_0}^t C_2(t') e^{i(\omega_o - \omega_k)(t-t')} dt'. \quad (4-7)$$

$C_2(t)$ depends upon the earlier value denoted by $C_2(t')$. To solve this equation, two assumptions are used [19]: the first one is the Markovian assumption which considers that the evolution of $C_2(t)$ is memory-less and therefore the integral over earlier times, namely $t' < t$, can be neglected. Then we simply replace $C_2(t')$ by $C_2(t)$ in eq. (4-7). Spontaneous radiative decay is very slow, as far as the atom is concerned, requiring millions of cycles of dipole oscillation before it is completed. Thus, the second assumption is to take $\exp[i(\omega_o - \omega_k)(t-t')]$ in eq. (4-7) as a fast oscillating function in the time interval given by $t-t_0$ so that

$$\int_{t_0}^t \exp[i(\omega_o - \omega_k)(t - t')] dt' = \pi \delta(\omega_o - \omega_k). \quad (4-8)$$

Using these two considerations, we have that the evolution of the excited state coefficient is given by

$$\frac{d}{dt} C_2(t) = -\frac{\pi \omega_o}{2\hbar} \sum_k |\boldsymbol{\mu} \cdot \mathbf{A}_k|^2 \delta(\omega_o - \omega_k) C_2(t) = -\Gamma C_2(t). \quad (4-9)$$

Then, the decay constant Γ is given by

$$\Gamma = \frac{\pi \omega_o}{2\hbar} \sum_k |\boldsymbol{\mu} \cdot \mathbf{A}_k|^2 \delta(\omega_o - \omega_k), \quad (4-10)$$

which, in the case of a continuous distribution of modes, can also be expressed as

$$\Gamma = \frac{\pi \omega_o}{2\hbar} \int d^3k |\boldsymbol{\mu} \cdot \mathbf{A}_k|^2 \delta(\omega_o - \omega_k). \quad (4-11)$$

This is the Wigner-Weisskopf theory of radiation, which predicts an irreversible decay of the population in upper state level with the subsequent production of photons. This irreversible decay corresponds to the exponential behavior result obtained for $C_2(t)$ in eq. (4-9).

4.3. Modification of Spontaneous Emission

Eq. (4-11) can be further modified to obtain a more useful result. We start by expressing the differential element d^3k in terms of the frequency differential as

$$d^3k = dS_\omega dk_\perp = dS_\omega \frac{dk_\perp}{d\omega} d\omega = dS_\omega \frac{1}{|\nabla_k \omega|} d\omega, \quad (4-12)$$

where dS_ω is an area differential element on a surface of constant frequency ω in the k space. Assuming that the interaction atom-field expressed by $|\boldsymbol{\mu} \cdot \mathbf{A}_k|^2$ depends only on the frequency and not on the value k , we can re-write the integral in eq. (4-11) as

$$\Gamma = \frac{\pi\omega_o}{2\hbar} \int d\omega |\boldsymbol{\mu} \cdot \mathbf{A}_\omega|^2 \delta(\omega_o - \omega_k) \int_{S_\omega} \frac{dS_\omega}{|\nabla_k \omega|}. \quad (4-14)$$

We recognize that the second integral is proportional to the Density of States [5], therefore the decay rate can also be expressed as

$$\Gamma(\omega_o) = \frac{\pi\omega_o}{2V\hbar} D(\omega_o) |\boldsymbol{\mu} \cdot \mathbf{A}_{\omega_o}|^2 \quad (4-15)$$

where V is the volume of the system considered. Eq. (4-15) is known as Fermi's golden rule of the transition rate of excited atoms. The decay rate Γ is also known as the emission probability per unit of time. This result indicates that the decay rate is not only a function of the density of photon states in the medium, but also a function of the interaction strength of the atomic dipole-field. In other words, the spontaneous emission phenomenon depends on the characteristics of the medium in which these atoms are immersed. The conclusions above were first analyzed by Purcell [20] and Kleppner [21] who stated that the emission rate could be altered by imposing nontrivial boundary conditions on the field.

4.4. Modified Photoluminescence Emission in Direct Band-Gap Semiconductors

We want now to extend the analysis of the spontaneous emission of a Two-Level Atom to the case of electronic transitions in direct bandgap semiconductors. These transitions may be modeled as a collection of atoms with different transition frequencies.

From the theory of emission of light in semiconductors, we have that the total emission rate as a function of the frequency of the photon is given by [22]

$$r_{sp} = \Gamma(\omega) N_J(\omega) f_n(E_2)(1 - f_p(E_1)) \quad (4-16)$$

where $\Gamma(\omega)$ is the emission probability described in the previous section, N_J is the joint density of states of electrons and holes, $f_n(E_2)$ is the probability of an electron to be at the energy level E_2 in the conduction band, and $f_p(E_1)$ is the probability of an electron to be at the energy level E_1 in the valence band. Substituting the value of the joint density of states and using the Boltzmann approximation for the energy distribution of both electrons and holes, the total emission rate is

$$r_{sp} = \Gamma(\omega) \frac{(2m_r^*)^{2/3}}{2\pi^2 \hbar^3} (\hbar\omega - E_g)^{1/2} e^{-\left(\frac{\hbar\omega - E_g}{k_B T}\right)} e^{-\frac{E_{fn} - E_{pn} - E_g}{k_B T}} \quad (4-17)$$

where $\Gamma(\omega)$ is give in eq.(4-15), m_r^* is the reduced mass of the electron-hole pair, E_g is the energy bandgap of the semiconductor, and E_{fn} , E_{pn} are the quasi-Fermi levels in the conduction and valence bands respectively. From eq. (4-17) it is evident that the spectral properties of the emitted light depend not only on the concentration of electron-hole pairs and the transition selection rules of the electron, but also on the photon density of states and dipole-field interaction. Typically, in solving for the light emitted by direct-bandgap semiconductors, the term Γ is assumed to be independent of the optical frequency. This assumption is valid only when the radiation occurs in unbounded medium, such as free space. In the case of eq. (4-17), a specific medium must be defined in order to establish the value of $\Gamma(\omega)$.

4.5. Radiation Spectrum from a 2D Photonic Crystal Cavity

We now describe the spectral properties of the light emitted by electron-hole pair recombination in the 2D photonic crystal cavity. When an electron-hole pair recombine in a photonic crystal cavity, as shown in Fig. (4.1), there are three different radiation modes into which the photon produced can be delivered: (a) the photon is delivered into the photonic crystal extended or leaky modes², (b) the photon couples into the cavity mode, and (c) the photon is delivered into free-space modes, i.e. it does not interact with the photonic crystal.

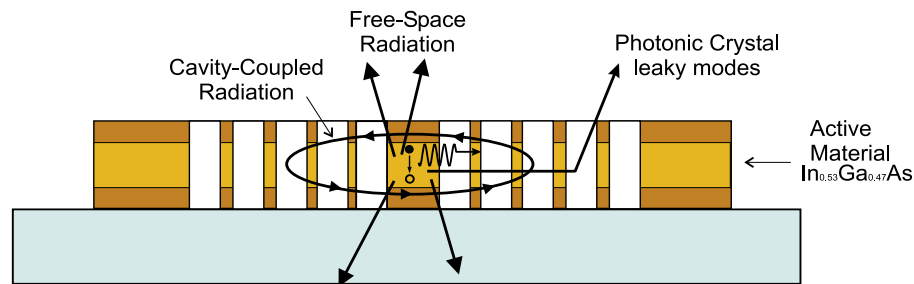


Figure 4.1: A photon is produced by electron-hole recombination inside the cavity region. The photon can be delivered into the photonic crystal leaky modes, the cavity mode, or the free-space radiation.

Since the photonic crystal has been designed to have a bandgap that covers most of the photoluminescence emission spectrum, we discard emission into the extended modes of the photonic crystal and only consider radiation into the cavity mode and the free-space modes. Then, the probability of emission can be expressed as a sum of both contributions, namely,

² See Appendix A

$$\Gamma(\omega) = \Gamma_{\substack{free \\ space}}(\omega) + \Gamma_{cavity}(\omega). \quad (4-18)$$

Thus, the emission rate in eq.(4-17) consists of radiation going into the cavity mode and into free-space modes, this is

$$r_{sp} = \left(\Gamma_{\substack{free \\ space}}(\omega) + \Gamma_{cavity}(\omega) \right) \frac{(2m_r^*)^{2/3}}{2\pi^2 \hbar^3} (\hbar\omega - E_g)^{1/2} e^{-\left(\frac{\hbar\omega - E_g}{k_B T}\right)} e^{-\frac{E_{fn} - E_{pn} - E_g}{k_B T}} \quad (4-19)$$

or,

$$r_{sp}(\omega) = r_{sp,free}(\omega) + r_{sp,cavity}(\omega) \quad (4-20)$$

The first term right-hand side of eq. (4-20) corresponds to the emission typical in light emitting diode structures while the second term is the rate of emission that goes into the cavity mode. To find the functional value of the spontaneous emission into the cavity, we model the density of states using a Lorentzian function. Then, from eq. (4-15) we have

$$\Gamma_{cavity}(\omega) = \frac{\pi\omega_o}{2V\hbar} \left| \boldsymbol{\mu} \cdot \mathbf{A}_{\omega_o} \right|^2 \frac{g}{2\pi\hbar} \frac{\Delta\omega}{(\omega - \omega_c)^2 + (\Delta\omega/2)^2} \quad (4-21)$$

where ω_c is the cavity's resonance wavelength and $\Delta\omega$ is the line-width.

4.6. Experimental Procedure and Setup

A semiconductor laser emitting at 780 nm is focused on the cavity by means of a microscope objective NA=0.85. The spot size of the focused light is of about 3 μm . In order to align the laser spot onto the cavity, the device was illuminated at the front side and imaged from the backside on a CCD camera. The sample was mounted on a Melles-Griot microblock translation stage, which allows positioning accuracy of about 0.3 μm .

The photoluminescence induced by the pump laser is collected at the backside of the sample by another microscope objective NA=0.85 and focused on the entrance slit of a SPEX Minimate 1681 monochromator. Two kinds of photodetectors were used to measure the filtered photoluminescence signal: a conventional InGaAs p-n heterojunction at room temperature and a liquid N₂ cooled Ge detector. The latter detector was used to extend the optical bandwidth relative to the InGaAs detector. The experimental setup is shown in Fig. (4.2).

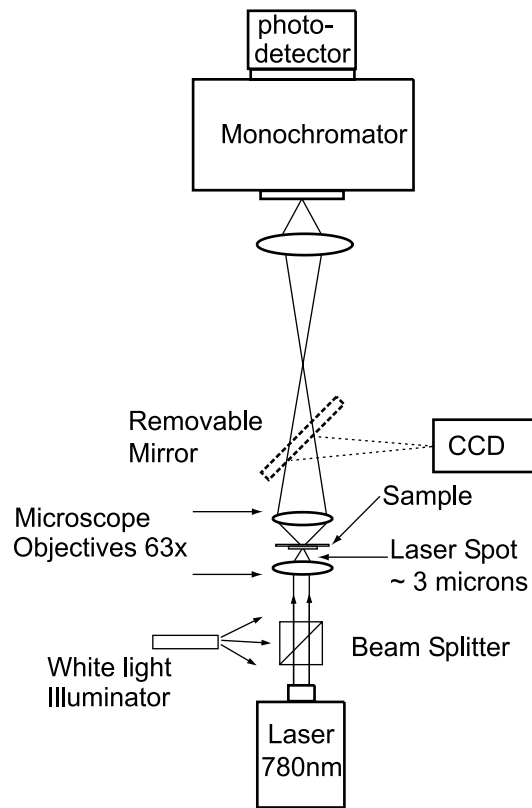


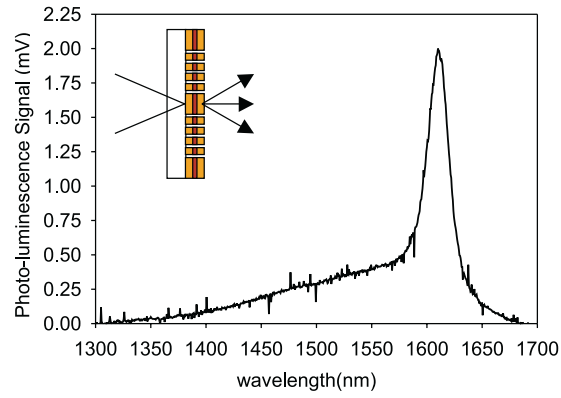
Figure 4.2: Experimental setup utilized in the photoluminescence characterization of the photonic crystal cavity.

4.7. Photoluminescence cavity signature and cavity tuning

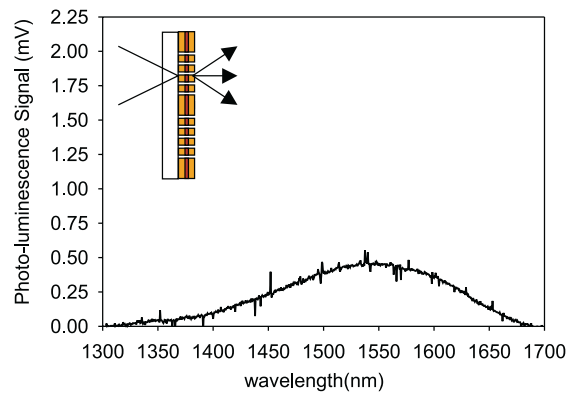
We induced photoluminescence at three different points of the sample: the cavity portion of the photonic crystal, the bulk portion of the photonic crystal, and the unpatterned region of the sample. The collected photoluminescence spectra are shown in Fig. (4.3). The cavity spectral signature is evident in the collected photoluminescence spectrum shown in Fig. (4.3)(a). This sharp feature, in contrast, is not present for the photoluminescence collected when the laser is focused away from the cavity. Fig. (4.3)(b), for example, shows the photoluminescence collected at a distance of 4 μm away from the cavity but still on the photonic crystal.

Do notice that there are no photonic crystal leaky modes present in the spectrum indicating that the photoluminescence spectrum lies inside the bandgap of the photonic crystal. These leaky modes are due to the coupling of the confined modes into radiation modes by means of the extended modes of the photonic crystal [17]. An overview of these modes is presented in Appendix A.

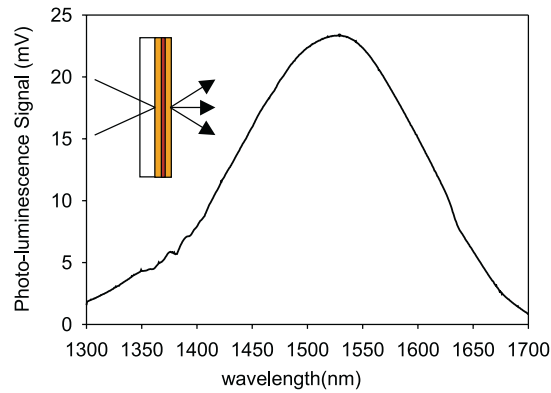
From Fig. (4.3) we can identify the two components of the photoluminescence spectrum described in eq. (4-20). The photoluminescence from the cavity consists of both components, $r_{sp,free}$ and $r_{sp,cavity}$, whereas the photoluminescence from the bulk photonic crystal consists only of $r_{sp,free}$. As expected, the signal level of $r_{sp,free}$ is the same for both cases is roughly the same.



(a)



(b)



(c)

Figure 4.3: Collected photoluminescence spectra when pump laser is focused on (a) cavity, (b) bulk photonic crystal ($4 \mu\text{m}$ from cavity), (c) unpatterned region.

The photoluminescence produced by the unpatterned region, which is shown in Fig. (4.3)(c) is significantly larger than that produced in the photonic crystal. The latter is due to several factors: the active material in the photonic crystal is less than it is in the unpatterned region, the photoluminescence emission is partially inhibited since it lies within the band gap of the photonic crystal, and the quantum efficiency is reduced due to the presence of edges and the occurrence of surface recombination.

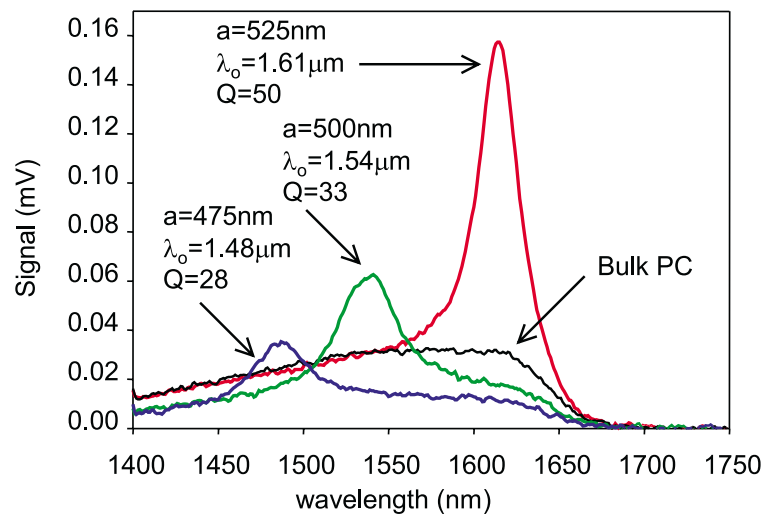


Figure 4.4: Photoluminescence spectra from cavities for different photonic crystal lattice parameters. The photoluminescence from the bulk photonic crystal is shown as reference. All the structures have the same void-filling factor of 35%. The signal fall off at the 1650 nm is due to the wavelength limit of the InGaAs photodetector used in this experiment.

The cavity resonant wavelength was tuned by fabricating structures with different lattice parameters. Fig. (4.4) shows the collected photoluminescence spectrum for the

fabricated devices. From this figure, the resonance wavelengths are 1480, 1540, and 1610 nm, which correspond to structures with lattice parameters of 475, 500, and 525 nm respectively. All these structures have roughly the same value of the resonance wavelength-lattice parameter ratio (λ_o/a) which is roughly 0.316. This value agrees with the design parameter obtained from numerical calculations [9].

4.8. Cavity Quality Factor Theory

The quality factor Q is the figure of merit in any confined system. The Q factor is related to the ability of any confined system to store energy. The Q factor is defined as

$$\frac{1}{Q} = \frac{P_l}{\omega_o W} \quad (4-22)$$

where ω_o is the optical frequency, W is the energy stored, and P_l is the power lost in one cycle. Since $1/Q$ is directly proportional to the energy loss rate of the confined system it is more convenient to the reciprocal Q .

The losses in the cavity are due to two mechanisms: radiation losses and absorption. The former refers to the energy that escapes from the cavity and the latter refers to power that is absorbed by the material inside the cavity. To quantify these two effects, we analyze a Fabry-Perot resonator that consists of two parallel mirrors [23]. One of the mirrors is 100% reflective whereas the other one has a reflectance close to a 100% but still allowing some light to leak out through transmission. The system is shown in Fig.(4-5). As indicated in this figure, P_+ and P_- correspond to the power of each counter-

propagating waves that constitute the standing wave inside the cavity, and P_e is the power that escapes from the cavity.

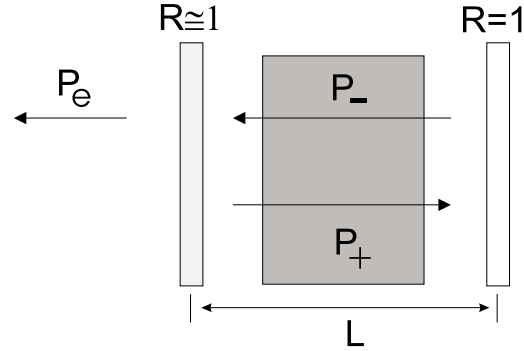


Figure 4.5: Fabry-Perot resonator filled with absorbing medium. The right side mirror is a perfect reflector whereas the left side mirror has a reflectivity very close to 1.

If we assume that the cavity is loss-less and the reflectivity of the mirrors is high, then the energy stored inside the cavity is divided half-and-half between each counter propagating wave. Thus, the power in the two counter-propagating waves is given by

$$P_{\pm} = \frac{1}{2} \frac{W}{L} v_g \quad (4-23)$$

where v_g is the group velocity of a wave inside the resonator and L is the length of the resonator. The power escaping through the partially reflecting mirror of transmittance T can be calculated as

$$P_e = TP_- = \frac{T}{2} \frac{W}{L} v_g \quad (4-24)$$

Using this result we can define radiation cavity Q or Q_{rad} as

$$\frac{1}{Q_{rad}} = \frac{P_e}{\omega_o W} = \frac{T v_g}{2 \omega_o L} \quad (4-25)$$

Now, we assume that the optical resonator is filled with a material that has an absorption coefficient α . Assuming that both counter-propagating waves experience the same loss, we have that the total power dissipated is given by

$$P_d = 4\alpha LP_{\pm} = 2\alpha Wv_g, \quad (4-26)$$

and, thus, the Q factor corresponding to absorption losses is

$$\frac{1}{Q_{abs}} = \frac{P_d}{\omega_o W} = \frac{2\alpha v_g}{\omega_o}. \quad (4-27)$$

Since $1/Q$ is proportional to the energy loss rate, we have that the total Q of the cavity can be obtained by adding eqs. (4-25) and (4-27), this is

$$\frac{1}{Q} = \frac{1}{Q_{rad}} + \frac{1}{Q_{abs}} = \frac{Tv_g}{2\omega_o L} + \frac{2v_g}{\omega_o} \alpha. \quad (4-28)$$

4.9. Separation of Radiation and Emission Losses in 2D Photonic Crystal Cavities

From Fig. (4.4), the factor Q corresponding to the different devices can be calculated as $Q = \Delta\lambda/\lambda$, where $\Delta\lambda$ is the full width at half maximum of each peak. Thus the measured Q factors of the structures are 50, 33, and 28 for the cavities whose resonance wavelengths are 1.61 μm , 1.54 μm , and 1.48 μm . As mentioned above, the factor Q is a function of the losses present in the cavity. These losses are due to absorption in the InGaAs layer and radiation losses. By plotting $1/Q$ versus different values of the absorption coefficient, it is possible to separate the two loss mechanisms.

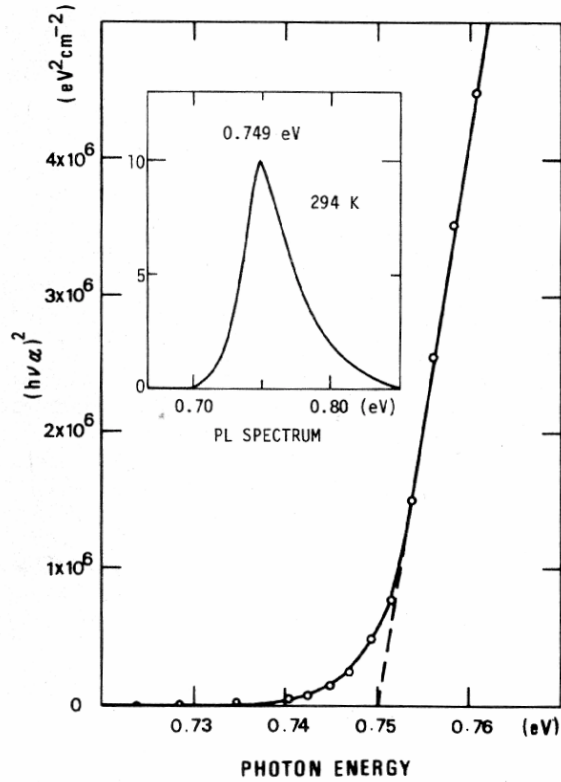


Figure 4.6: Measured absorption coefficient [24] as a function of the photon energy in $\text{In}_{0.47}\text{Ga}_{0.53}\text{As}$. The intersection of the dashed line with the abscissa corresponds to the energy bandgap. The photoluminescence spectrum of the sample studied is shown in the inset.

Fig. (4.6) shows the absorption spectrum for the $\text{In}_{0.47}\text{Ga}_{0.53}\text{As}$ alloy [24]. We can interpolate values for the absorption coefficient from this plot using the following equation based on a parabolic density of states:

$$\alpha(\hbar\omega) = 20493.0 \frac{1}{\hbar\omega} \sqrt{\hbar\omega - 0.75} \quad (\text{cm}^{-1}) \quad (4-29)$$

where $\hbar\omega$ is expressed in eV. We can use eq. (4-29) to obtain the value of the absorption coefficient corresponding to each cavity resonance in Fig. (4.4) and plot $1/Q$ versus the absorption coefficient. This plot is shown in Fig. (4.7).

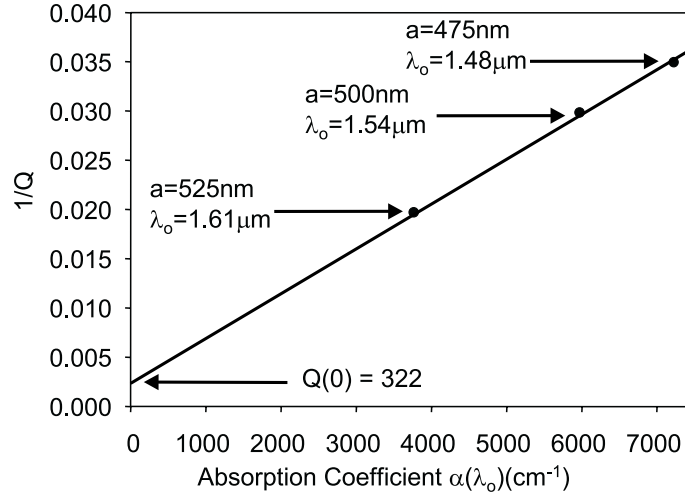


Figure 4.7: Cavity quality factor $1/Q$ vs. absorption coefficient obtained from the data of Fig. (4.4). The photonic crystal lattice parameter is a and the cavity resonance wavelength is λ_o .

This plot agrees well with the model proposed in eq.(4-28). From the linear extrapolation to the case of zero absorption, we find that $Q_{\text{rad}} \approx 320$. This value of Q agrees well with that calculated in references [9, 25]. Higher- Q values have been recently reported for more sophisticated designs, using quantum dot luminescent semiconductors that have very low average absorption coefficients [15, 16].

Notice that eq. (4-28) is a slight function of the frequency and, thus, the plot in Fig. (4.7) should not have to be a straight line. Furthermore, the value of Q_{rad} is also a function of the frequency. This situation, however, was not taken into account since the

change in the optical frequency is of about 7% whereas the absorption coefficient increases by a factor of two for the same frequency range.

5. Characterization of 2D Photonic Crystal Cavities by Elastic Scattering Measurements.

5.1. Introduction

As mentioned in the previous chapter, photoluminescence has been the most common experimental procedure to analyze 2D photonic crystal devices. One of the main advantages of this procedure is the fact that the light is produced inside the structure, thereby allowing a very efficient coupling into the electromagnetic modes present in the photonic crystal device. To access the highest possible Q , it is desirable to fabricate such devices in passive materials, i.e. those which do not produce light either by photon or carrier excitation. In order to characterize device made in passive media, light from a tunable source is sent into the structure and the scattered radiation is measured for different values of the wavelength. Since the light that is sent into the cavity has the same frequency with the light that scatters from it, the process is called elastic scattering.

Elastic scattering is widely used in many experiments involving the characterization of small particles and surfaces [26]. In the majority of these experiments, the scattering properties of a single particle are obtained from the scattering of a collection of them, particularly by measuring the extinction coefficient as a function of the wavelength. In this work, we determine the scattering properties by addressing a single "particle" or scattering element, which in this case is the cavity in the 2D photonic crystal. As shall be seen in this chapter, the spectral resonance and the spatial

confinement of the cavity electromagnetic mode is evident in the spectrum of the scattered light.

5.2. Experimental Setup for Elastic Scattering

Fig. (5.1) depicts the basics of the experimental procedure to measure elastic scattering of light from 2D photonic crystal cavities. The experiment consists of measuring the light scattered by the cavity when a tunable source is focused on it. The light interacts with the structure, is scattered in every direction, and is measured by a photodetector. To decrease the intensity of the background light, the photodetector is placed so that it measures the off-axis back scattered light. Then, by tuning the source along a range of wavelengths, the scattering spectrum is obtained. The scattering signature from the cavity is found by comparing the spectra obtained when the light is focused on the cavity versus when it is focused on the bulk photonic crystal.

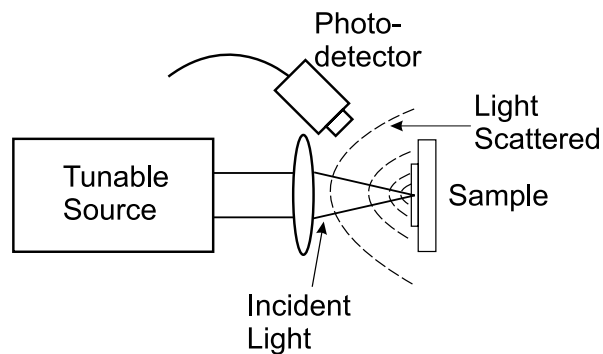


Figure 5.1: Basic experimental setup for measuring elastic scattering.

Several issues needed to be overcome in order to carry out this experiment properly. Firstly, the incident light has to be focused down to a spot size comparable to

the size of the cavity, i.e. down to several microns at the most. In the case of photoluminescence characterization, this was not problematic, as the pump laser wavelength was 780nm and the photoluminescence signal was strong enough. For elastic scattering, the source has to be tuned to the resonance wavelength of the device, which lies in the 1.55 μm regions. This is roughly twice the wavelength of the laser used in the photoluminescence experiment and, thus, will double the spot size in a diffraction limited optical system.

Another experimental issue is the alignment of the focused incident light onto the cavity. Chromatic aberration does not allow the infrared light and the visible light used for alignment. Thus, an optical setup similar to that shown in Fig.(4.2) cannot be used. Furthermore, since the dimensions of the cavity are on the order of half a micron, it cannot be effectively imaged with light in the 1.55 μm range.

Fig. (5.2) depicts the experimental setup used to measure the elastic scattering including the focusing alignment hardware. A New Focus 6300 tunable laser was focused on the sample by means of a long working distance microscope objective NA=0.45. The measured spot size was of 4.5 μm . The laser can be tuned to any wavelength within 1511nm to 1570nm, which corresponds to the so-called *conventional* or C band in optical telecommunication systems. The focal point of the incident laser was verified by imaging the reflected light onto an Electrophysics 7290A lead-sulfide IR camera.

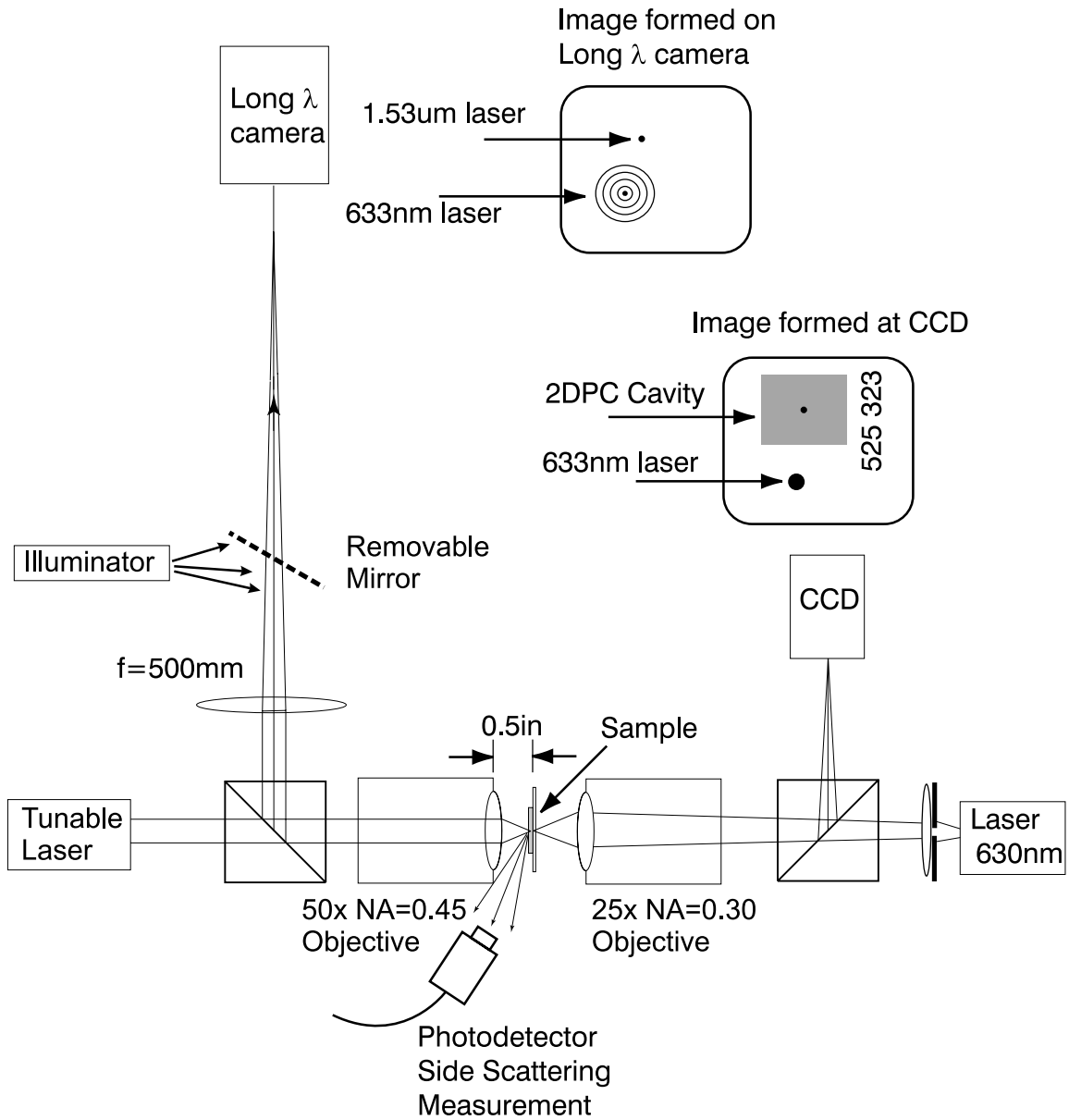


Figure 5.2: Complete experimental setup for elastic scattering measurements. The sample is sandwiched by two long working distance microscope objectives. The light from an illuminator is sent through the system to image the devices on two cameras. The two insets show the images seen on CCD camera and on long wavelength camera prior to alignment.

As mentioned, chromatic aberration in the optics prevents the infrared laser and the visible image of the structured to be in focus at the same time on the long λ camera. This limits the ability of positioning (or aligning) the laser spot right on the cavity, which is $\approx 600\text{nm}$ in diameter. To properly position the IR laser spot on the cavity, a visible laser at 630 nm is focused on the backside of the sample by means of a long working distance microscope objective $\text{NA}=0.3$. The focusing is verified by imaging the reflected light on a CCD camera. Since the 630nm laser light is in the visible region, the laser spot and the 2D PC cavity can now be imaged on the CCD at the same time. In Fig. (5.2), the image formed at the CCD camera is shown. Both infrared and visible lasers appear now on the long λ camera. By adjusting the objectives, the visible laser is aligned to the infrared laser using the image formed on the long λ camera. Having both lasers focused at the same position on the sample, the cavity can now be effectively aligned to the infrared spot using the image formed at the CCD. This alignment technique proved to be effective to align infrared light to particles as small as $1.5\mu\text{m}$ in diameter. It was noted, however, when aligning to a cavity, there is a position error of about $0.5\mu\text{m}$. The latter was not a severe limitation of the setup as the sample could be finely repositioned to achieve a higher scattering signal from the cavity.

5.3. Elastic Scattering Spatial Mapping

We use the experimental setup depicted in Fig. (5.2) to obtain the scattering signal from the cavity. The tunable laser was set to a wavelength close to the resonance of one of the cavity structures and measurements of the scattering were taken at different points

around the cavity. Fig. (5.3) shows the map of the scattering near the cavity. A drawing of the photonic crystal is shown in the background of the plot. The structure analyzed had a lattice parameter of 500nm, a hole radius of 310nm, and a resonance wavelength of 1540nm, as seen in the previous chapter. Since the spot size was of about 4 microns, the measured spatial mode distribution is influenced by the mode spatial extent and the spot size. The scattering peak at the cavity measured was 1.22 times the signal size of the background from other parts of the photonic crystal. In relative numbers, the measured background was 2mV whereas the measured peak was 2.44mV. It is noted that the background signal came from the stray light in the sample.

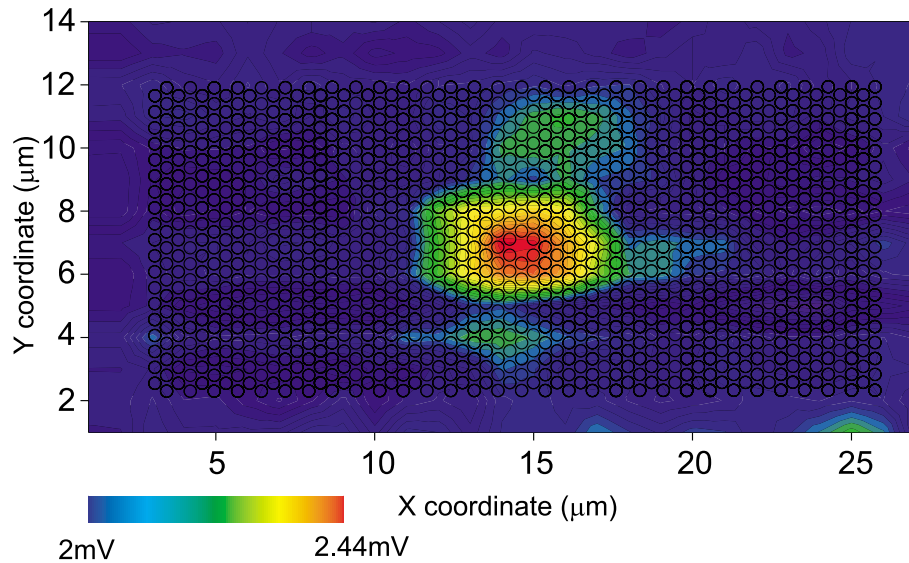


Figure 5.3: Scattering spatial map of the electromagnetic defect mode using light at 1.54 μm. The 2D photonic crystal cavity is drawn at scale in the background as a reference. The device studied has a lattice period $a=500$ nm and a void filling factor of 35%.

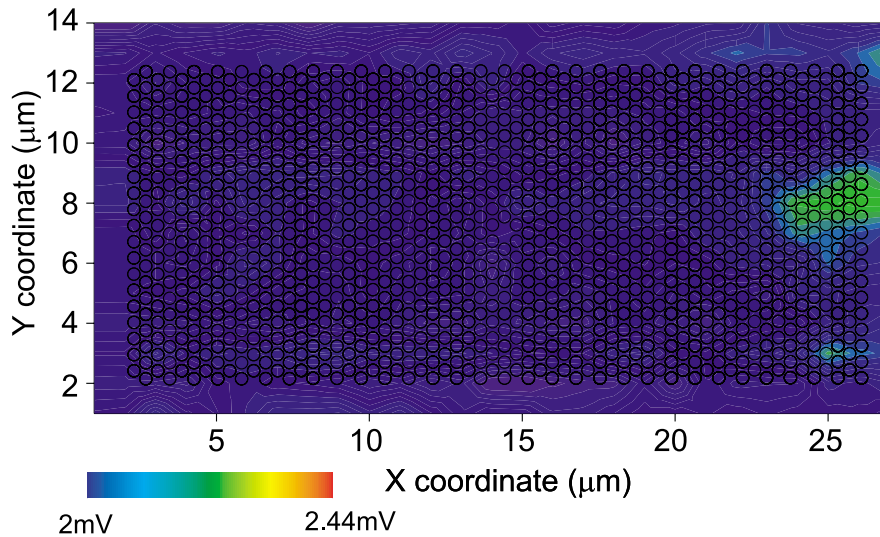


Figure 5.4: Same as Fig. 5.3 but for a device with lattice period $a=525$ nm and a void filling factor of 35%. No resonance is measured in this case.

For the sake of experimental consistency, Fig. (5.4) shows the scattering map obtained from a different photonic crystal cavity using the tunable laser set to the same wavelength used to obtain Fig. (5.3). In this case, the device had a lattice parameter of 525nm and a resonance wavelength of 1610nm. As expected, no scattering is observed in the vicinity of the cavity. A similar result is obtained for the structure with lattice parameter of 475nm, as its resonance wavelength is at 1480nm.

It is interesting to notice that scattering can be obtained by illuminating any kind of obstruction or localized obstacle whose size is comparable to the wavelength. The photonic crystal cavities analyzed in this section can also be thought as a localized obstacle of comparable sizes. Indeed, the physical sizes of the cavities in Fig. (5.3) and in

Fig. (5.4) differ just by tens of nanometers; they, however, produce very different results in scattering which indicates the influence of the sharp optical resonance induced by the photonic crystal.

5.4. Scattering from 2D photonic crystal cavity compared to other objects

For comparison to the scattering produced by 2D photonic crystal cavities, we performed the same scattering experiment with other objects such as a particle of about 1.5 μm in diameter and an isotropic scattering surface. The former was obtained from grit on sample while the latter was obtained from a rough white surface that produces only diffuse reflection. The measured scattering signal produced by the particle was 6 times larger than that of the cavity. The measured scattering signal produced by the isotropic scattering surface was 57 times larger than that of the cavity.

5.5. Elastic Scattering Spectrum

Fig. (5.5) shows the measured scattering signal as a function of the wavelength. The wavelength range is limited by the tunable laser. The measured device had a lattice parameter of 500nm and a hole radius of 310 nm. Two spectra were taken: the scattering spectrum when laser was focused on the cavity, and on the defect-free photonic crystal. The latter can be regarded as a background signal. As expected, the scattering produced by the cavity is wavelength dependent and is maximum at the resonance wavelength,

which is around 1549 nm. The signal strength in both cases increases due to the spectral characteristics of the tunable laser.

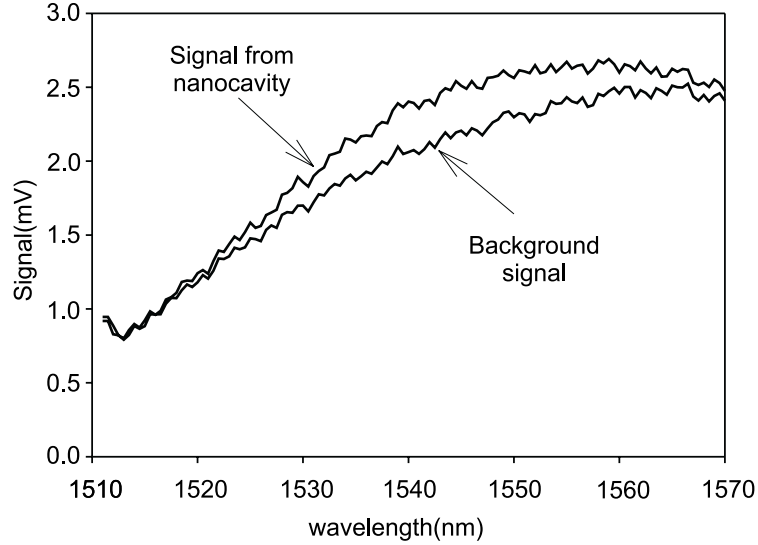


Figure 5.5: Scattering signal from cavity and background signal. The overall increase of the signal as a function of wavelength observed in both cases is due to the spectral response of the tunable laser. The device studied has a lattice period $a=500$ nm and a void filling factor of 35%.

Fig. (5.6) shows the scattering strength relative to the background. This is the difference of the background and the scattered signal divided by the background. From this figure, we notice that the cavity Q measured by elastic scattering is ≈ 40 , which is close to what was measured in photoluminescence (see Fig. 4.4). As mentioned in the previous chapter, this value of Q is the result of radiation and absorption losses in the device. The spectrum shown in Fig. (5.6) demonstrates that the elastic scattering method is perfectly suitable to characterize 2D photonic crystal cavities.

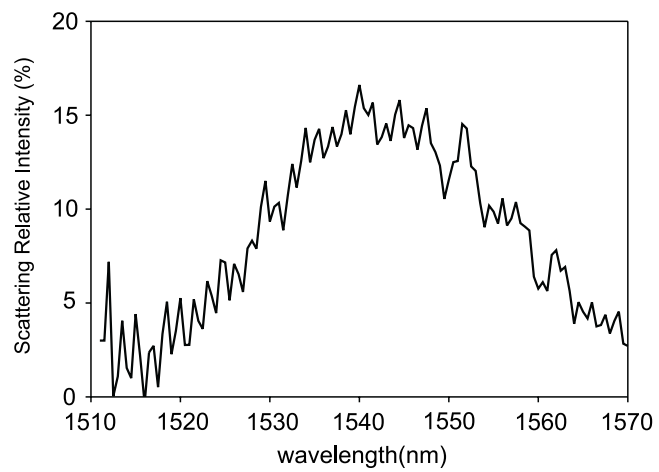


Figure 5.6: Cavity's scattering spectrum relative to the background from the data shown in Fig. 5.5.

6. Summary and Suggestions for Future Work: Prospects for Increasing Cavity Q.

6.1. Summary

We have designed, fabricated and characterized two-dimensional photonic crystal single defect cavities. These devices could constitute a building block for photonic integrated circuits based on two-dimensional photonic crystals.

The cavities were designed according to numerical simulations obtained from different sources. The design parameters of the structure were chosen to have an operation wavelength in the range used in optical fiber telecommunications.

A fabrication procedure was developed for these devices. Such fabrication involved the use of sub-micron lithography, dry etching, and wet etching techniques. The overall procedure was optimized in different ways in order to obtain high quality structures. Since the process is fundamentally planar and within the reach of industrial photolithography, it is well suited for commercial micro-fabrication.

The signature of the cavity was observed in the spectrum of photoluminescence. Cavities with different resonance wavelengths were tested. Cavity resonance wavelengths covering the optical C band were obtained. The cavity quality factor Q was measured and a model for the separation of the different loss mechanisms was presented. The measured values of the cavity resonance wavelength and the cavity quality factor agree well with the theoretical values.

Finally an alternative experimental method to characterize two-dimensional photonic crystal single defect cavities was proposed. This method relies on the elastic scattering of light exhibited by the device that could lead to much higher measured Q-factors since absorption would be absent. The experimental results obtained by this technique are in agreement with those obtained by photoluminescence. This method can be potentially used to characterize passive single defect cavities, i.e. those that are made on non-absorbing media. Non-absorbing media are more likely to be found in photonic integrated circuits made for applications such as wavelength division multiplexing, and for achieving the highest possible Q.

6.2. Prospects for Increasing Cavity Q: Selective Modification of Defect's Dielectric Constant

As mentioned in Chapter 2, the confinement in the cavity is provided by the photonic crystal in the horizontal direction and by total internal reflection in the vertical direction. The total degree of confinement is given by the loss rate in the vertical direction plus the loss rate in the horizontal direction, and, thus, the total Q can be calculated using the following equation

$$\frac{1}{Q} = \frac{1}{Q_{\perp}} + \frac{1}{Q_{\parallel}} \quad (6-1)$$

where $1/Q_{\perp}$ and $1/Q_{\parallel}$ represent losses in the vertical and horizontal directions respectively and the absorption losses have been neglected. The Q_{\parallel} is increased by the number of cells in the photonic crystal surrounding the cavity while the Q_{\perp} can be

controlled by locally changing the dielectric constant in the cavity. Fig. (6.1) shows a 2D photonic crystal cavity in which the cavity dielectric constant has been locally modified.

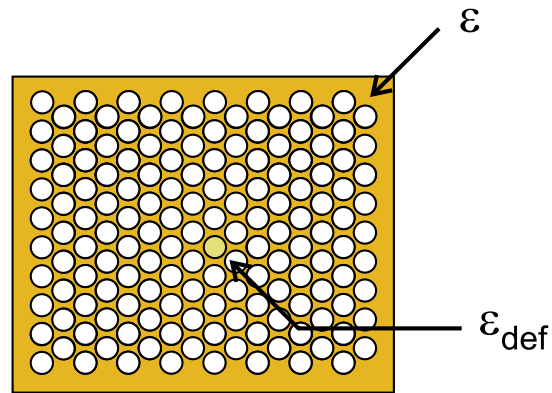


Figure 6.1: Photonic crystal defect cavity with modified dielectric constant.

It has been shown theoretically that reducing the value of the dielectric constant of the defect increases the confinement [9] and, thus, increases the value of the quality factor Q . In Fig. (6.2) the calculated energy stored in the cavity is plotted as a function of time. The quality factor Q is estimated from the energy temporal decay exhibited. From Fig. (6.2), it can be seen that there is a substantial increase in the cavity Q from 210 to 1050 as the cavity dielectric constant is reduced from 11.56 to 4.

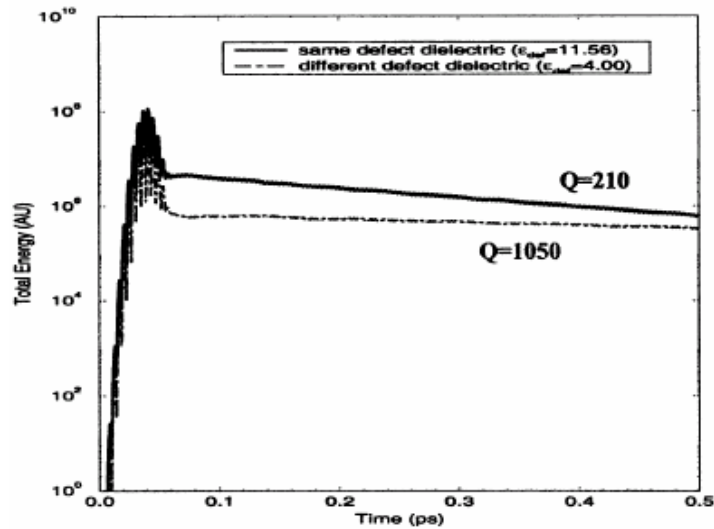


Figure 6.2: Calculated energy stored in the cavity as a function of time. Reduction of the dielectric constant decreases the temporal decay of the energy stored [9].

The value of 4 for the dielectric constant is the optimum and further reduction will again decrease the cavity Q of the device. It is important to mention that changing locally the cavity dielectric constant will also change the resonance wavelength. Further redesign of the geometry of the structure will be required to achieve the right operation wavelength.

Several experimental techniques have been developed to locally modify the dielectric constant of semiconductor materials. In the case of III-V semiconductors, Quantum Well Intermixing can be used for this purpose. This method commonly uses a SiO₂ layer to promote the out diffusion of Ga, creating and diffusing vacancies during a thermal annealing process. This can also be applied to the InP material system with the

use of an InGaAs cap on which the SiO₂ layer is deposited. The initial steps of fabrication process steps are shown in Fig. 6.3. After these steps are done, the fabrication process continues as described in Chapter 3 of this thesis.

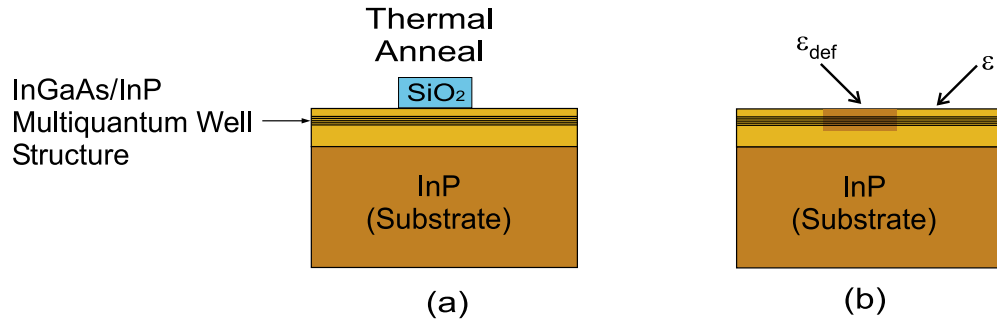


Figure 6.3: Quantum-Well intermixing process. (a) A SiO₂ film is patterned on top of an InGaAsP/InP multiple quantum well structure. The wafer is then thermally annealed. (b) The SiO₂ film is removed. The dielectric constant of the structure is locally modified.

One of the disadvantages of this process is the fact that the change in the dielectric constant is smaller than what is theoretically required to obtain a dramatic increase in the quality factor Q of the cavity. Typical changes in refractive index induced by quantum well intermixing are of about 10% which means that the dielectric constant of the material could be reduced from 11.56 to 11 only [27]. Another disadvantage is the fact that the photonic crystal cavity needs to be fabricated on a quantum well material structure.

Another alternative to locally changing the dielectric constant of a photonic crystal cavity is to switch to the Silicon-On-Insulator (SOI) material system. Indeed, SOI has recently been used to produce photonic integrated circuits. In SOI, there is a method

called Separation by Ion Implantation of Oxygen (SIMOX). In this technique, ions of Oxygen are implanted onto a silicon substrate and SiO₂ is formed by thermally annealing. By masking the substrate accordingly, isolated regions of oxide can be formed. Fig. 6.4 depicts the initial process steps followed in SIMOX. After these steps, the process continues as described in Chapter 3.

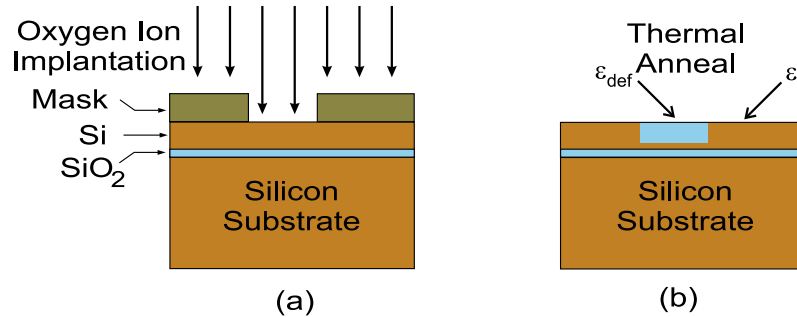


Figure 6.4: The SIMOX process. (a) Oxygen ions are implanted on a masked SOI wafer. (b) The mask is removed and the wafer is thermally annealed. SiO₂ is formed in the exposed regions.

With this method, it is possible to reduce the dielectric constant from 11.56 to 2.56, closer to what is theoretically required. Furthermore, the use of silicon as a material system can take advantage of the well-developed industry expertise and technology.

Appendix A: Extended Modes in 2D Photonic Crystal Films

In this appendix, the so-called extended or leaky modes in 2D photonic crystals are reviewed. It is important to mention that these modes and their behavior have been studied extensively and lie at the core of the research that has been carried out in the field of photonic crystals. The review of the extended modes presented in this section is limited to those encountered in 2D photonic crystal structures similar to those studied in this dissertation. A detailed explanation of these modes and how to measure them can be found in [17].

As mentioned in this thesis, the defect modes in 2D photonic crystal cavities are spatially localized electromagnetic waves whose frequency lies in the forbidden bandgap. In addition to the defect mode, which is only present when there is a defect of some sort in the periodic structure, there are also the extended modes. These electromagnetic modes are those with frequency lying in the allowed propagation band, as was briefly mentioned in Chapter II. One of the main properties of the extended modes is the fact that, as their name implies, they extend and propagate throughout the entire photonic crystal structure.

One way to characterize the extended modes in 2D photonic crystals is to measure the angle-resolved photoluminescence spectrum. To understand how this works, let us consider a laser pumping a thin layer of photoluminescent semiconductor material. The emission produced can escape right out of the film, if it lies within the escape cone, or it can stay trapped inside the structure, if it lies outside this cone. The latter corresponds to

light trapped in the guided modes of the structure. This is shown in Fig. (A.1)(a). If a photonic crystal is carved into the semiconductor thin film, the light that would otherwise be trapped interacts with the photonic crystal and is sent out of the film by Bragg diffraction at a particular angle, as seen in Fig. (A.1)(b). Since these modes escape out from the film, they are also called leaky modes. The scattering angle is strongly dependent on the frequency of the emitted light, as we shall see shortly. Tracking the emission frequency peaks at different angles is the basis of characterizing the extended modes in 2D photonic crystals. Do notice that, in order to excite the extended modes by photoluminescence, the photonic crystal must be designed such that the luminescence spectrum lies precisely within the allowed propagation spectral band.

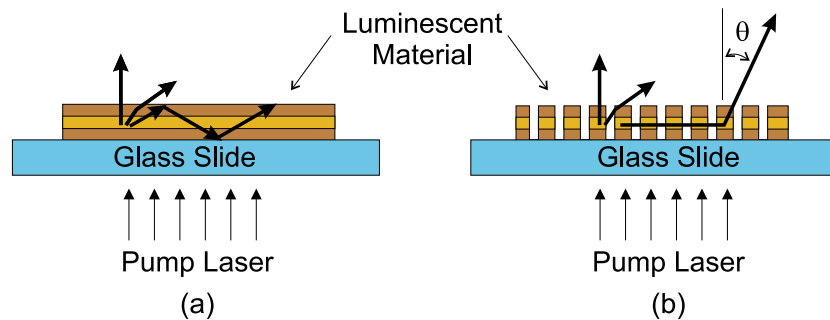


Figure A.1: Emission from a thin layer of photoluminescent material on a glass slide. The material can be the structure InP/InGaAs/InP studied in this thesis. (a) unpatterned thin film: part of the emission escapes while part is trapped; (b) thin film photonic crystal: the emission that is trapped can be extracted by Bragg diffraction.

A sketch of the experimental setup is shown in Fig. (A.2). This setup is similar to that used in the photoluminescence characterization of the cavities shown in Fig. (4.2). The

main difference is that, in order to observe the modes, spatial filtering is required along with spectral filtering. In Fig. (A.2), the structure is pumped by a laser and the induced photoluminescence is collected by a lens. The distance between the structure and the lens is set to be the focal length. The collimated signal is then filtered in order to discriminate over the spectrum of the light emitted at different angles or values of the wavevector.

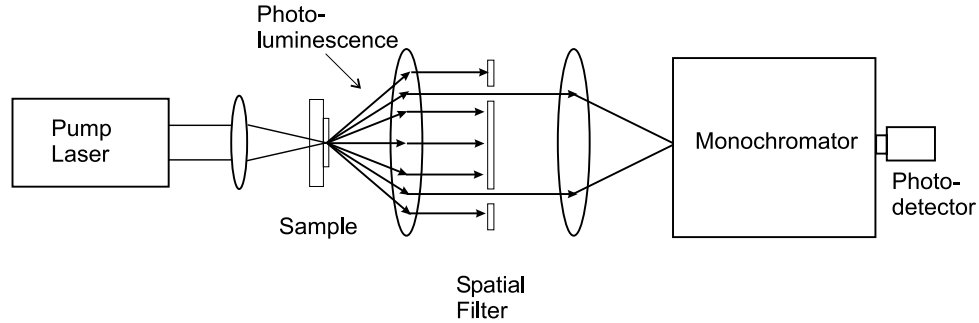


Figure A.2: Experimental setup for angle-resolved photoluminescence.

The sample is pumped with a laser and the emission is collected on the opposite side. A spatial mask is used to select the angle.

A typical spectrum of the angle-resolved photoluminescence is shown in Fig. (A.3). In this case, the angle was 35° . The two polarization modes can be further distinguished by setting a polarizer right before the monochromator in Fig. (A.3). The spectrum shown was taken from a thin film 2D photonic crystal triangular structure with lattice period of $a = 720\text{nm}$. Do notice that the lattice parameter is larger than that of the structures studied in this thesis. This particular choice of the lattice parameter ensures that most of the photoluminescence spectrum lies in the allowed propagation band of the photonic crystal.

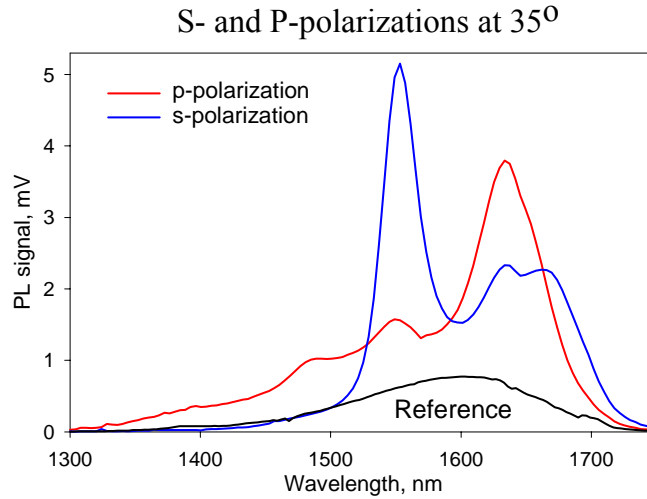


Figure A.3: Typical spectra obtained using angle-resolved photoluminescence. The spectra show the difference in polarization state of the emitted light. The reference is the photoluminescence obtained from the unpatterned semiconductor thin-film.

As can be evidenced from the figure, the angle-resolved spectrum has several peaks at different values of the frequency. These peaks correspond to occurrences of Bragg diffraction at different frequencies but at the same diffraction angle. The angle can be associated to a particular value of the wavevector of the light in the reduced Brillouin zone. Thus, the photonic band structure can be mapped out by tracking the evolution of these peaks at different angles and finding their corresponding wavevector. Fig. (A.4) shows a typical dispersion map wherein the peaks from the angle-resolved spectrum in Fig. (A.3), along with those spectra at other angles, have been used.

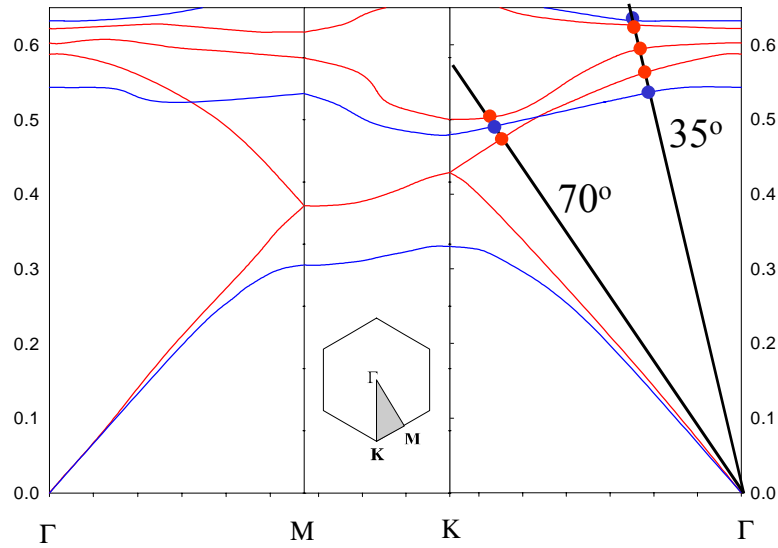


Figure A.4: Map of the dispersion characteristic of the extended modes.

The inset shows the Brillouin zone of the studied 2D photonic crystal.

As seen from Fig. (A.4), different modes can be mapped out by properly spatial-filtering the photoluminescence. Since the photonic crystal is two dimensional, the mask used in Fig. (A.2) does not possess azimuthal symmetry and it has to be set in different positions to map out the different directions of the Brillouin zone.

As can be seen from Fig. (A.3), the overall signal strength obtained from the photonic crystal is larger than that obtained from the unpatterned semiconductor, which implies that the light extraction efficiency has been increased. One of the promising applications of the extended modes in 2D photonic crystals is, precisely, the increase of light extraction from LED structures.

Bibliography

- [1] E. Yablonovitch, 'Inhibited Spontaneous Emission in solid-state physics and electronics,' Phys. Rev. Lett. **58**, 1110 (1987).
- [2] J.D. Joannopoulos, R.D. Meade, J. N. Winn, 'Photonic Crystals: Molding the Flow of Light', Princeton University Press, Princeton, NJ, 1995.
- [3] H. Kosaka, T. Kawashima, A. Tomita, M. Notomi, T. Tamamura, T. Sato, S. Kawakami, 'Superprism Phenomena in Photonic Crystals: Toward Microscale Lightwave Circuits', J. Lightwave Technol. **17**, 2032 (1999).
- [4] M. Boroditsky, R. Vrijen, T. Krauss, R. Coccioli, R. Bhat, and E. Yablonovitch, 'Spontaneous Emission Extraction and Purcell Enhancement from Thin-Film 2-D Photonic Crystals' J. Lightwave Technol. **17**, 2096 (1999).
- [5] N. W. Ashcroft, N.D. Mermin, 'Solid State Physics' Saunders College, Philadelphia, PA, 1976.
- [6] M. Plihal and A. A. Maradudin, 'Photonic Band Structure of two-dimensional systems: the triangular lattice', Phys. Rev. B. **44**, 8565-8571 (1991).

- [7] R. Coccioli, M. Boroditsky, K.W. Kim, Y. Rhamat-Samii, E. Yablonovitch, 'Smallest possible electromagnetic mode volume in a dielectric cavity' *Proc. IEE Proc.-Optoelectron.* **145**, 391 (1998)
- [8] O. Painter, J. Vuckovic, A. Scherer, 'Defect modes of a Two-Dimensional Photonic Crystal in an Optically Thin Dielectric Slab', *J. Opt. Soc. Am. B* **16**, 275 (1999).
- [9] H. Mossallaei, Ph.D. Dissertation Thesis, University of California, Los Angeles, CA, 2001.
- [10] R. Williams, 'Modern GaAs Processing Methods', Artech House, Boston, 1990.
- [11] T. Krauss, R. de la Rue, and S. Brand, 'Two-dimensional photonic bandgap structures operating at near-infrared wavelegnth's' *Nature* (London) **383**, 699 (1996).
- [12] C. Cheng, A. Scherer, R. Tyan, Y. Fainman, G. Witzgall, and E. Yablonovitch, 'New fabrication techniques for high quality photonic crystals', *J. Vac. Sci. Technol. B* **15**, 2764, (1997).

- [13] A. Scherer, O. Painter, B. D'Urso, R. Lee, and A. Yariv, 'InGaAsP photonic band gap crystal membrane microresonators', *J. Vac. Sci. Technol. B* **16**, 3906 (1998).
- [14] C. Smith, S. Murad, T. Krauss, R de la Rue, and C. Wilkinson, *J. Vac. Sci. Technol. B* **17**, 113 (1999).
- [15] C. Smith, R.M. de la Rue, M. Rattier, S. Oliver, H. Benisty, C. Weisbuch, T. Krauss, R. Houdre, and U. Oesterle, *Appl. Phys. Lett.* **78**, 1487, (2001)
- [16] T. Yoshie, A Scherer, H. Chen, D. Huffaker, and D. Deppe, *Appl. Phys. Lett.* **79**, 114, (2001).
- [17] M. Boroditsky, R. Vrijen, T. Krauss, R. Coccioli, R. Bhat, and E. Yablonovitch, *J. Lightwave Technol.* **17**, 2096 (1999)
- [18] W.D. Zhou, J. Sabarinathan, P. Bhattacharya, B. Kochman, E. Berg, P. Yu, and S. Pang, *IEEE J. Quantum Electron.* **37**, 1153, (2001).
- [19] L. Allen and J. H. Eberly, 'Optical Resonance and Two-Level Atoms', JohnWiley & Sons Inc., New York, 1975.
- [20] E. M. Purcell, *Phys. Rev.* **69**, 618 (1946).

- [21] D. Kleppner, Phys. Rev. Lett. **47**, 4, 233 (1981).
- [22] P. Bhattacharya, 'Semiconductor Optoelectronics', Prentice Hall, Upper Saddle River, NJ, 1993.
- [23] H. Haus, 'Waves and Fields in Optoelectronics', Prentice Hall, Englewood Cliffs, NJ, 1984.
- [24] Y. Takeda, A. Sasaki, Y. Imamura, and T. Takagi, J. Appl. Phys. **47**, 5405 (1976).
- [25] P. Villeneuve, S. Fan, S. Johnson, and J. Joannopoulos, IEE Proc. Optoelectron. **145**, 384 (1998).
- [26] C.F. Bohren and D.R. Huffman, 'Absorption and Scattering of Light by Small Particles' Wiley Interscience
- [27] L. Zhan, K.S. CHan, E.Y.B. Pun, and H.P. Ho, 'Wavelength Shift Enhancement in Quantum-Well Intermixed Distributed-Feedback Lasers', IEEE Photon. Technol. Lett. **14**, 6 (2002) 744